NASA Contractor Report 191495

STRATOSPHERIC AIRCRAFT EXHAUST PLUME AND WAKE CHEMISTRY

R.C. Miake-Lye, M. Martinez-Sanchez, R.C. Brown,
C.E. Kolb, D.R. Worsnop, M.S. Zahniser, G.N. Robinson
J.M. Rodriguez, M.K.W. Ko, R-L. Shia, N.D. Sze,
C.W. Heisey, L. Fox, S.C. Wofsy, and P. Davidovits

AERODYNE RESEARCH, INC.
Billerica, Massachusetts

Contract NAS1-19161
July 1993

(NASA-CR-191495) STRATOSPHERIC
AIRCRAFT EXHAUST PLUME AND WAKE
CHEMISTRY (Aerodyne Research)
65 p

N94-12572

Unclas

G3/46 0179686

National Aeronautics and
Space Administration

Langley Research Center
Hampton, Virginia 23681-0001

ARI-RR-1006

STRATOSPHERIC AIRCRAFT EXHAUST PLUME AND WAKE CHEMISTRY

Prepared by

R.C. Miake-Lye, M. Martinez-Sanchez, R.C. Brown, C.E. Kolb,
D.R. Worsnop, M.S. Zahniser, and G.N. Robinson
Aerodyne Research, Inc.
45 Manning Road
Billerica, MA 01821

J.M. Rodriguez, M.K.W. Ko, R-L. Shia, N.D. Sze and C.W. Heisey
Atmospheric and Environmental Research, Inc.
840 Memorial Drive
Cambridge, MA 02139

L. Fox and S.C. Wofsy
Department of Earth and Planetary Sciences
Harvard University
Cambridge, MA 02138

P. Davidovits
Department of Chemistry
Boston College
Chestnut Hill, MA 02167

Prepared for

Atmospheric Effects of Stratospheric Aircraft
High Speed Research Program
Contract NAS1-19161
NASA Langley Research Center
Hampton, VA 23681-0001

TABLE OF CONTENTS

Chapter 1

MODEL SIMULATIONS OF HETEROGENEOUS CONDENSATION BEHIND AN HSCT AIRCRAFT

INTRODUCTION

It is now recognized that heterogeneous reactions on polar stratospheric cloud particles and lower latitude stratospheric sulfuric acid droplets can amplify catalytic cycles by which chlorine active compounds destroy ozone. Field measurements have demonstrated that ClO levels can be enhanced by heterogeneous chemistry acting on polar stratospheric clouds during early winter and spring.[1] Heterogeneous mechanisms have also been shown to play an important role in the mid-latitude stratosphere where atmospheric models based solely on homogeneous chemistry underpredict the observed ozone decrease at mid- and high- latitudes.[2-3] It is interesting to note, for example, that model simulations which include the reaction

$$N_2O_5 + H_2O \text{ ---> } 2HNO_3 \qquad (1)$$

acting on global sulfate aerosol layer indicate a decreased sensitivity of ozone to the injection of nitrogen oxides compared to two-dimensional models which include only gas phase chemistry.[4]

The potential impact of heterogeneous chemistry on stratospheric ozone depletion has indicated a need to assess the environmental consequences of exhaust particulates from high altitude aircraft. Such an evaluation is particularly important to current efforts to predict the environmental perturbations which would result from a fleet of High Speed Civil Transport (HSCT) aircraft which would fly between 15-23 km.[5] Exhaust particulates can effect stratospheric chemistry by perturbing the local ambient concentration of condensation nuclei or by inducing condensation in water vapor rich plumes. In the latter case, plume condensates may directly catalyze key atmospheric reservoir species reactions or act as catalysts for heterogeneous reactions which change exhaust levels of odd nitrogen species. Simulations designed to investigate the relative importance of these processes require predictive models for contrail formation and condensation kinetics.

In earlier work, plume and wake dynamics, mixing and chemistry behind an HSCT aircraft were investigated using estimated emissions for a prototypical HSCT engine.[6] Treatment of the plume chemistry focused on the evolution of NO_x, including ozone oxidation mechanisms and conversion to HNO_3, as well as SO_x oxidation mechanisms. Additionally, water vapor condensation was treated by assuming thermodynamic equilibrium between vapor and condensed phases.

Equilibrium condensation predictions should provide reasonable estimates for the onset of condensation and an upper limit for the overall mass balance of condensate. However, to assess the potential impact of heterogeneous chemistry in the plume and wake, a more detailed description of the condensation process is required. This includes, accurate estimates for the number density, size distribution and chemical characteristics of exhaust particulates, realistic descriptions of particulate activation mechanisms, reliable models for contrail particle droplet growth, and accurate rate parameters for heterogeneous reactions between gas phase plume species and condensate.

In this paper, our earlier modeling work[6] is extended to include the kinetic model for heterogeneous condensation of plume gases developed by Hoshizaki, et. al.[7,8] in the late 1970's. Although originally developed to predict rocket plume visibility, the model is equally applicable to heterogeneous condensation phenomena associated with expansion and dilution processes in high altitude aircraft plumes. In the present work, this model is used to investigate the parametric dependence of contrail droplet sizes on the number density and size distribution of exhaust condensation particles. Model simulations for an HSCT flying in the lower stratosphere than provide some qualitative guidelines for the potential size distribution of droplets formed in HSCT contrails.

HETEROGENEOUS CONDENSATION

Kinetic Condensation Model

Heterogeneous condensation is treated using the kinetic model developed by Hoshizaki, et. al.[6,7] to predict plume visibility under flight conditions. In this model, condensation is treated as a kinetic process of aerosol droplet growth on pre-existing solid nuclei particles in the plume and/or ambient free-stream. Condensation nuclei may be water insoluble, soluble or mixed and particle growth occurs by vapor diffusion with a kinetic correction for small drops. Coalescence of drops is neglected.

The condensation model is based on the formalism of Fukuta and Walter[9] for droplet growth by vapor diffusion. In particular, the growth of individual droplets is given by

$$\frac{d\mu_{\alpha,i}}{dt} = \left(\frac{4\pi r_i^2}{RT}\right) x \frac{D_\alpha W_\alpha (p_{\alpha,i} - e_{\alpha,i})}{\left[\frac{D_\alpha}{\beta_\alpha}\left(\frac{2\pi W_\alpha}{RT}\right)^{1/2} + \frac{r_i}{\lambda_i / r_i}\right]} \qquad (2)$$

where α refers to a condensible vapor component (e.g. H_2O, HNO_3, etc.) and the subscript i refers to the i-th droplet which is distinguished by its core radius and chemical type (i.e. soluble, insoluble or mixed). In Equation 2, t is time, $\mu_{\alpha,i}$ is the mass of α on the i-th droplet, r_i is the droplet radius, β_α is the condensation coefficient, W_α is the molecular weight, γ_i is the mean free path, D_α is the molecular diffusion coefficient, $p_{\alpha,i}$ is the local plume partial pressure, and $e_{\alpha,i}$ is the saturation vapor pressure. The saturation vapor pressure depends on the chemical composition and radius of the droplet. For example, for single component condensation on an insoluble exhaust nuclei, $e_{\alpha,i}$ is given by the classical Kelvin equation

$$e_{\alpha,i} = e_{\alpha,\infty} \exp\left[\frac{2W_\alpha \sigma_i}{RT_i r_i}\right] \qquad (3)$$

In Equation 3, e_α is the saturation vapor pressure of α over a plane solution surface of the same composition as the drop, p_i is the particle density, T_i is the particle surface temperature and σ_i is the surface tension of the aqueous solution against air.

The growth equations defined by Equation (2) are integrated along a set of pseudo-streamlines corresponding to the center streamline of a streamtube of constant exhaust mass flux. Normalized steamlines are defined in terms of the plume flowfield thermodynamic parameters by

$$\psi(R) = \frac{\int_0^R \chi_e \rho U r dr}{\int_0^\infty \chi_e \rho U r dr} \tag{4}$$

where χ_e is the exhaust mass fraction, p is the plume density and U is the velocity. For the simulations presented below, the plume flowfield speciation and gas dynamic properties were determined using the Standard Plume Flowfield Model, SPF-2.[10]

For a given pseudo-streamline, the kinetic condensation calculations start at the equilibrium saturation point represented by the saturation temperature, T_s, and pressure, p_s. At this point each core nuclei is considered initially coated by an infinitesimal liquid layer. Thus, the only model criterion for activation is that the nuclei has the critical size needed for growth given by

$$\frac{p_{\alpha,i}}{e_{\alpha,i}} > 1 \tag{5}$$

There are two key approximations in this model. First, since particle growth is followed along average streamlines, particle diffusion across streamlines is neglected. Second, depending upon the physical and chemical characteristics of the exhaust particulates, the current model can overestimate the number of active condensation nuclei. Hallett, et. al.,[11] for example, has shown that only as much as 2% of freshly burned JP4 may be activated.

Comparison with Equilibrium Predictions

In earlier work, the SPF-2 code was modified to predict water vapor condensation during the plume expansion using the standard vapor pressure test for thermodynamic equilibrium. Model simulations were performed for three cases and the condensation predictions were compared against condensation predictions based on Appleman's[12] equilibrium, fully-mixed condensation algorithm. These same cases have been treated here using the kinetic condensation overlay. The condensation predictions from all three approaches are summarized in Table 1. It can be seen that the three approaches are in general agreement. Based on these results, the remainder of this paper will focus on case 3 for which all three approaches predicted contrail formation.

Table 1. Summary of H_2O Condensation Predictions

latitude	N47	N47	N85
altitude (km)	18.40	17.85	18.30
date	June 15	January 1	January 1
temperature (K)	219.	216.7	205.2
pressure (atm)	0.0734	0.0712	0.0573
SPF-2 equilibrium condensation	no	no	yes
fully-mixed equilibrium condensation	never	uncertain	always
kinetic condensation	no	no	yes

Plume Flowfield Mixing and Chemistry

The standard plume Flowfield code, SPF-2, was used to characterize the chemical and physical properties of the near- and far-field exhaust plume. Model simulations used estimated emissions for a hypothetical MACH 2.4 engine[13] to specify exit plane exhaust speciation and 1990 atmospheric conditions[14] to specify the ambient atmospheric speciation, temperature and pressure as a function of latitude and altitude. A more detailed discussion of these calculations, including a listing of the reaction set used to simulate finite-rate chemistry in the mixing region, is given in Reference 5.

To implement the kinetic condensation model overlay, the flowfield viscous mixing region is first subdivided into streamshells characterized by a constant flux of exhaust mass. The droplet growth equations are then integrated along the centerline of each streamshell. Plume gas dynamic properties along each streamline are obtained by interpolation using the full flowfield solution.

Five pseudo-streamlines and temperature field obtained by interpolation for case 3 in Table 1 are shown in Figure 1. The shaded area defines the region in which the equilibrium condensation model predicted no condensation. Condensation initially occurs in the outer boundary of the plume due to relatively rapid dilution and subsequently spreads towards the plume axis at longer times. The time and axial distance at which saturation is obtained are displayed in Figures 2a and 2b, respectively, as a function of streamline. These figures indicate condensation throughout the plume within approximately 0.7 sec and at an axial distance of approximately 1500 ft downstream of the nozzle exit plane.

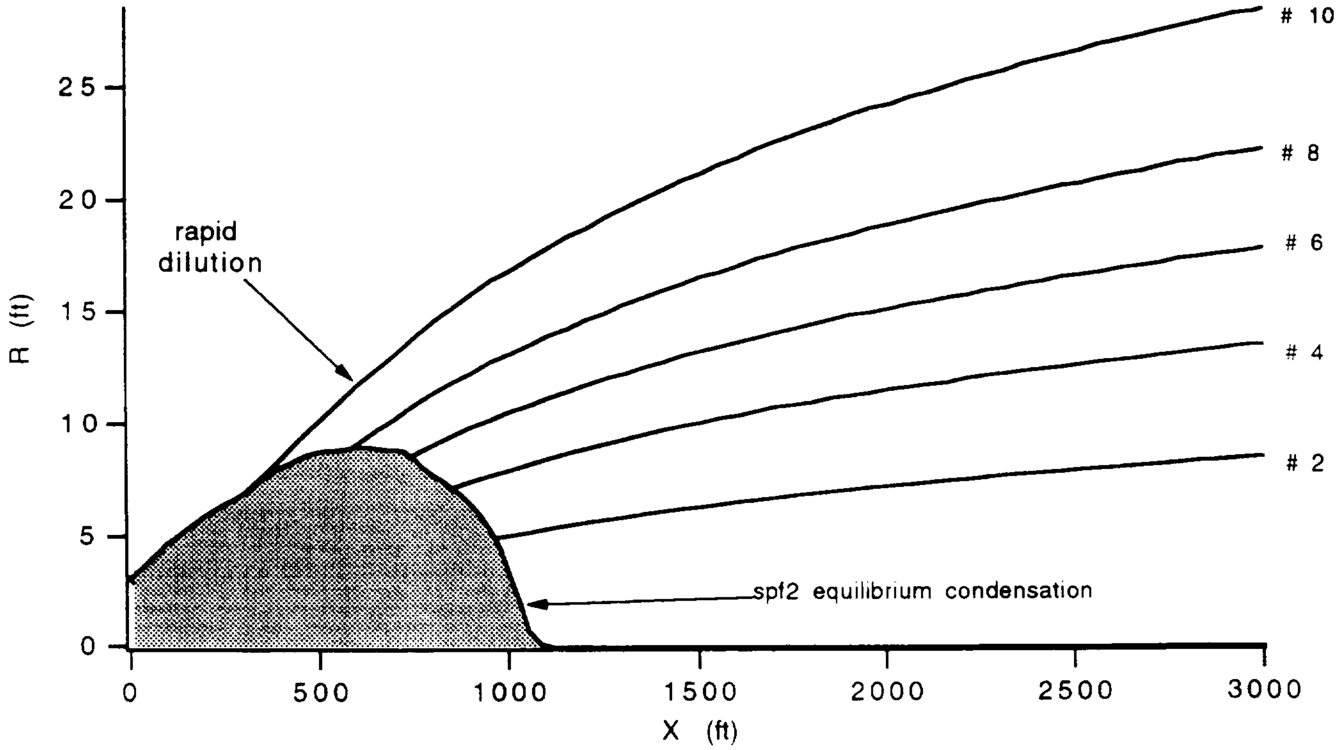

Fig. 1: Pseudo-streamlines (a) and temperature profiles (b) for a hypothetical Mach 2.4 HSCT at a latitude of N85 and an altitude of 18.3 km. Ambient conditions correspond to January 1990 atomospheric conditions.

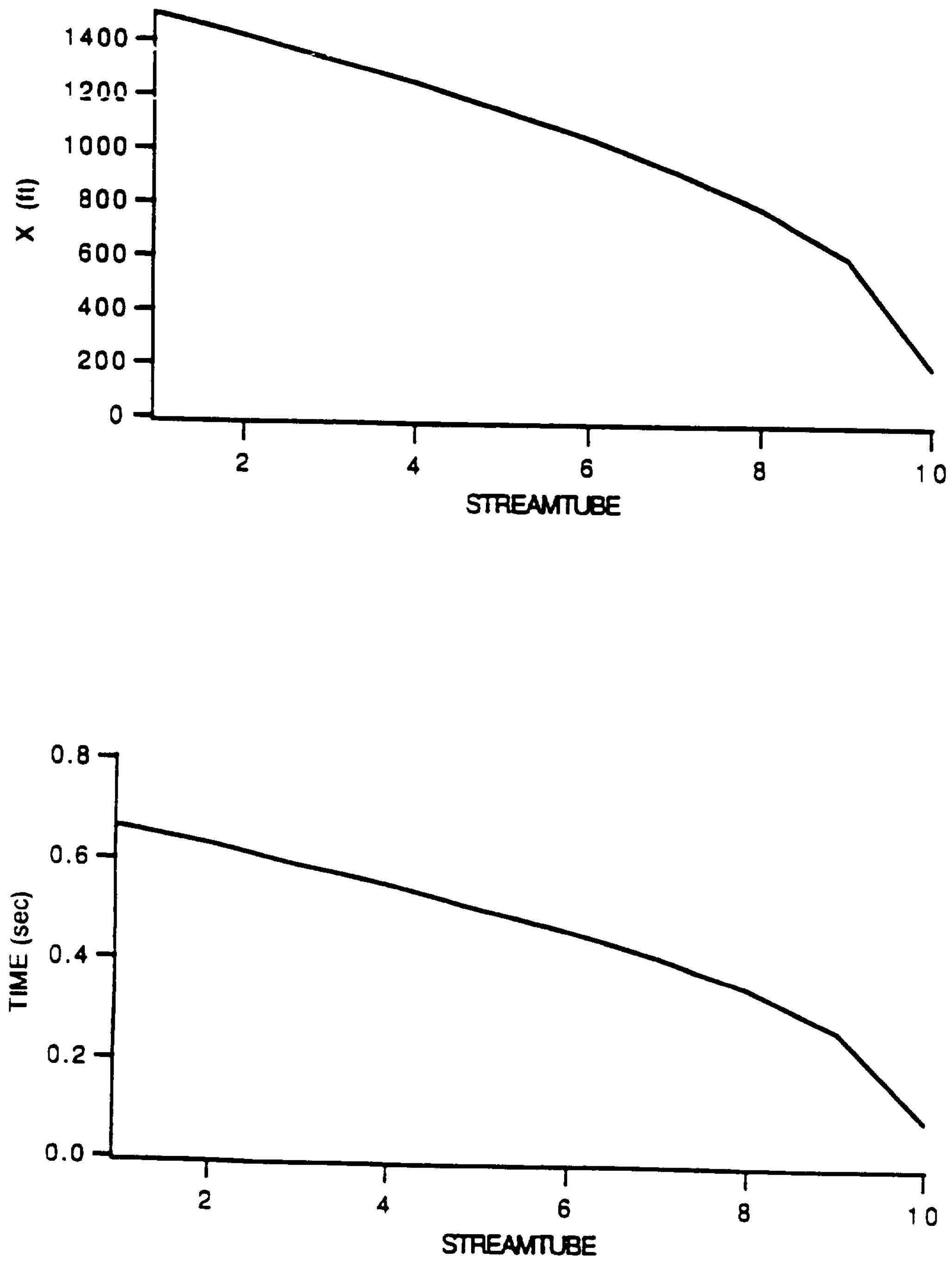

Fig. 2: Time and axial distrance at which saturation is reached as a function of streamline.

Exhaust Particulate and Condensation Nuclei Distribution

Since HSCT engines are still under development, exhaust particulate emissions are unknown. More over, very little is known about the nucleating properties of turbojet and turbofan propelled aircraft operating in the upper troposphere and/or lower stratosphere in general. Experimental measurements of the number density and size distribution of jet engine exhaust particulates or the fraction which become active condensation nuclei have been rather sparse and fundamental work on activation mechanisms is largely nonexistent.

In this paper, it is assumed that the insoluble soot particles are the primary exhaust particulates. A base exhaust particulate distribution is then adopted which is qualitatively consistent with existing measurements for jet aircraft exhausts. The parametric dependence of contrail particle growth on the number density and size distribution is then illustrated by model simulation for various perturbations to this base case.

Figure 3 displays two particle spectrums treated in the present work. The base distribution (distribution 1) is illustrated by the shaded histogram. This distribution approximates the particulate distribution observed by Low, et. al.[15] for a Pegasus engine burning JP5 and is also generally consistent with other observations.[16-20] The second (unshaded) distribution (distribution 2) assumes a smaller average particle size than the base case. The shape, however, is similar to the base distribution except for a faster falloff in number density for large particle radii. The same exhaust particulate mass loading is used for each distribution. Consequently, particulate number densities are significantly larger for the shifted distribution.

To illustrate the effect of exhaust particulate number density, a third distribution (distribution 3 - not shown) will also be considered. This distribution is identical to the base (shaded distribution in Figure 3) case except that the exhaust particulate mass fraction (and, therefore, number density) is reduced by two orders of magnitude.

The condensation model assumes that at the saturation point along a given streamline exhaust particulates are initially coated by an infinitesimal layer of condensate. In this sense, all exhaust particulates are active condensation nuclei and will subsequently grow as long as Equation (4) is satisfied. Consequently, comparing the condensation kinetics for distributions 1 and 2 illustrates the effect of shifts in the activated CN size distribution for a constant exhaust mass loading. Comparing the condensation kinetics for distributions 1 and 3, on the other hand, can be viewed as comparing contrail formation assuming 100% of the exhaust particulates are activated to contrail formation assuming 1% of the insoluble particulates are activated.

Water Vapor Condensation Simulations

Figures 4-6 display the mass fraction of condensed H_2O as a function of axial distance for the three distributions described in Section 2.4. Results for the base distribution are shown in Figure 4. Results for distributions 2 and 3 are shown in Figures 5 and 6, respectively. In each case, results are shown for three selected pseudo-streamlines from Figure 1. In progressing from streamline # 2 through # 10, the streamlines are moving from near the plume axis towards the plume/ambient boundary. Collectively, therefore, these profiles illustrate the affects of both the local plume environment and exhaust CN distribution on the extent of condensation.

Comparing the profiles for each of the three streamlines illustrates (see Figure 2) that condensation first occurs in the other edges of the plume and, subsequently extends in towards the plume axis further downstream. Since the equilibrium saturation point for a given streamline

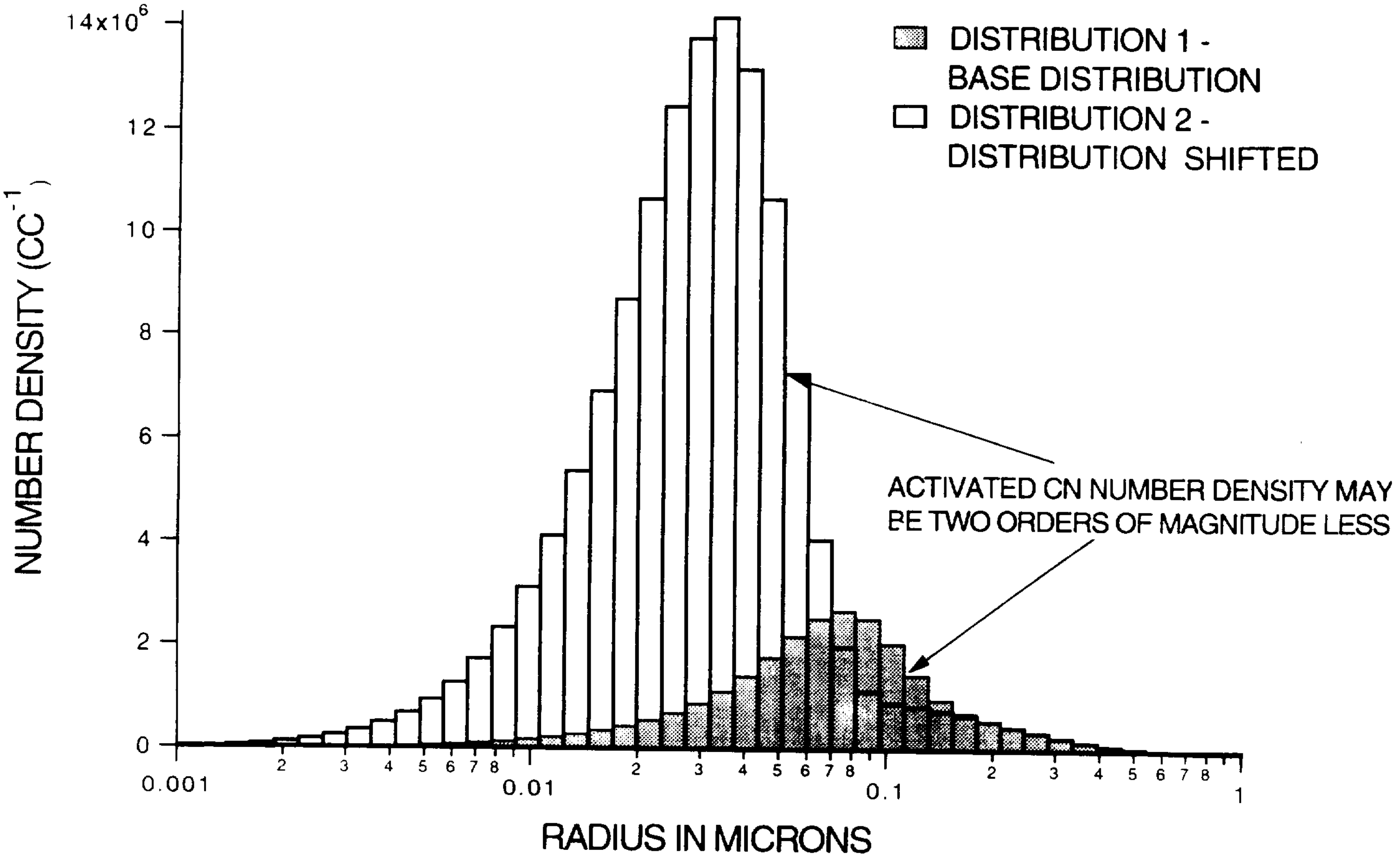

Fig 3: Insoluble exhaust particulate distributions used in simulation HSCT contrail formation. Distribution #1 corresponds to the base distribution and is in qualitative agreement with measurements for typcial jet aircraft engines. Distribution # 2 assumes the same exhaust particulate masss fraction, but is shifted to smaller radii and exhibits a faster fall-off at larger radii. The number of insoluble exhaust particulates which are active condensation nuclei may be two orders of magnitude smaller.

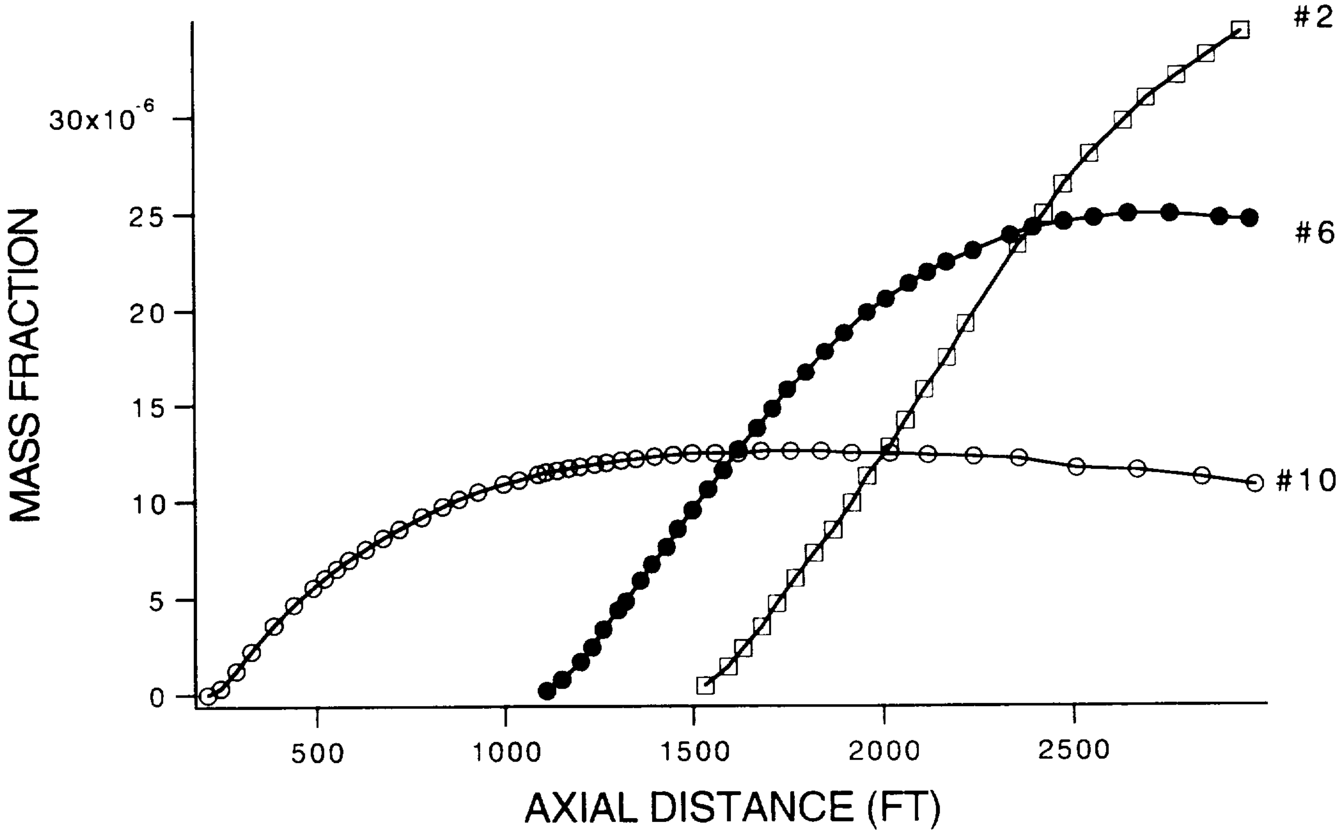

Fig 4: Condensed H_2O mass fraction as a function of plume axial distrance for the base exhaust particulate distribution assuming 100% of the particulates are activated condensation nuclei. Results are shown for contrail droplet growth along three different flowfield stramlines (#2 - near plume axis; # 6 - midway between plume axis and plume/ambient boundary; # 10 - near plume ambient boundary).

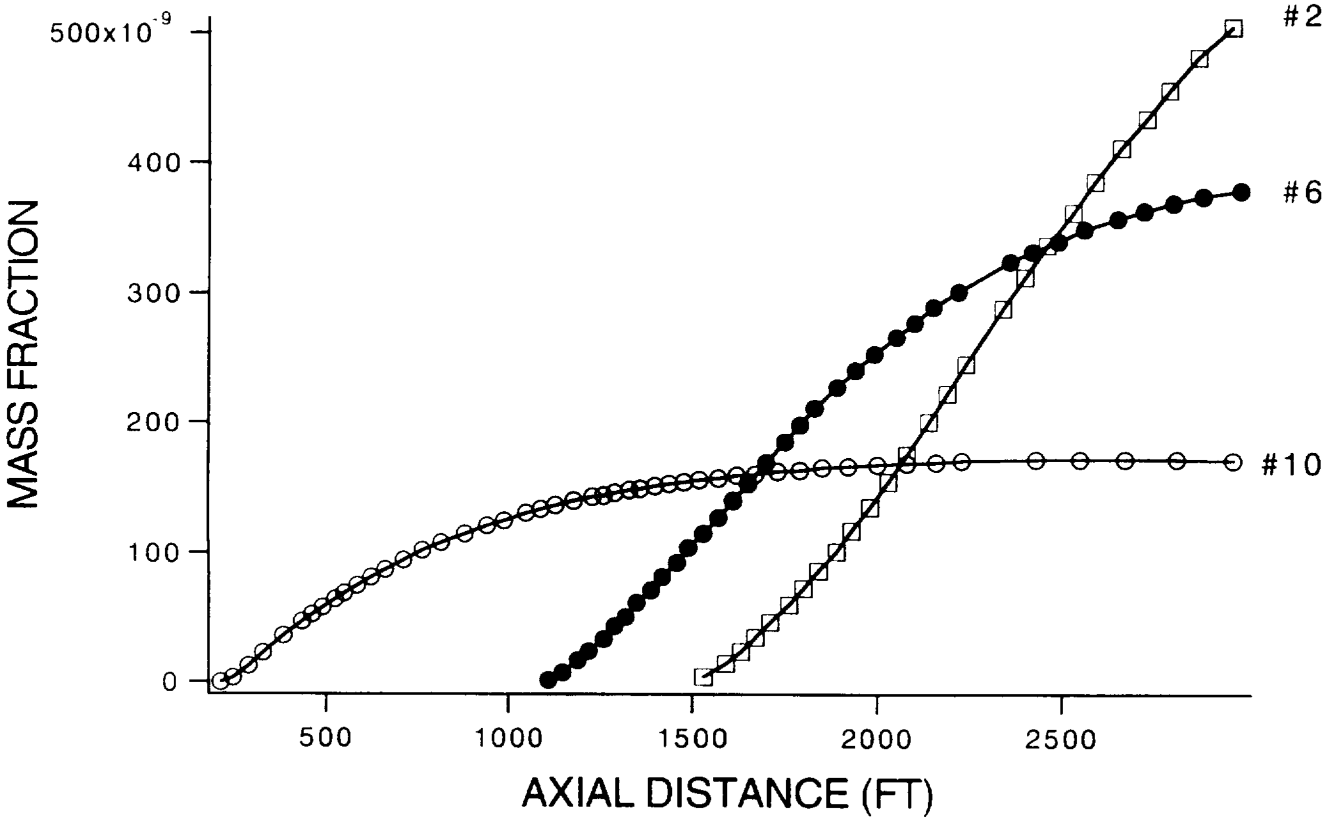

Fig. 5: Condensed H_2O mass fraction as a function of plume axial distrance for the base exhaust particulate distribution assuming 1% of the particulates are activated condensation nuclei. Results are shown for contrail droplet growth along three different flowfield stramlines (#2 - near plume axis; # 6 - midway between plume axis and plume/ambient boundary; # 10 - near plume ambient boundary).

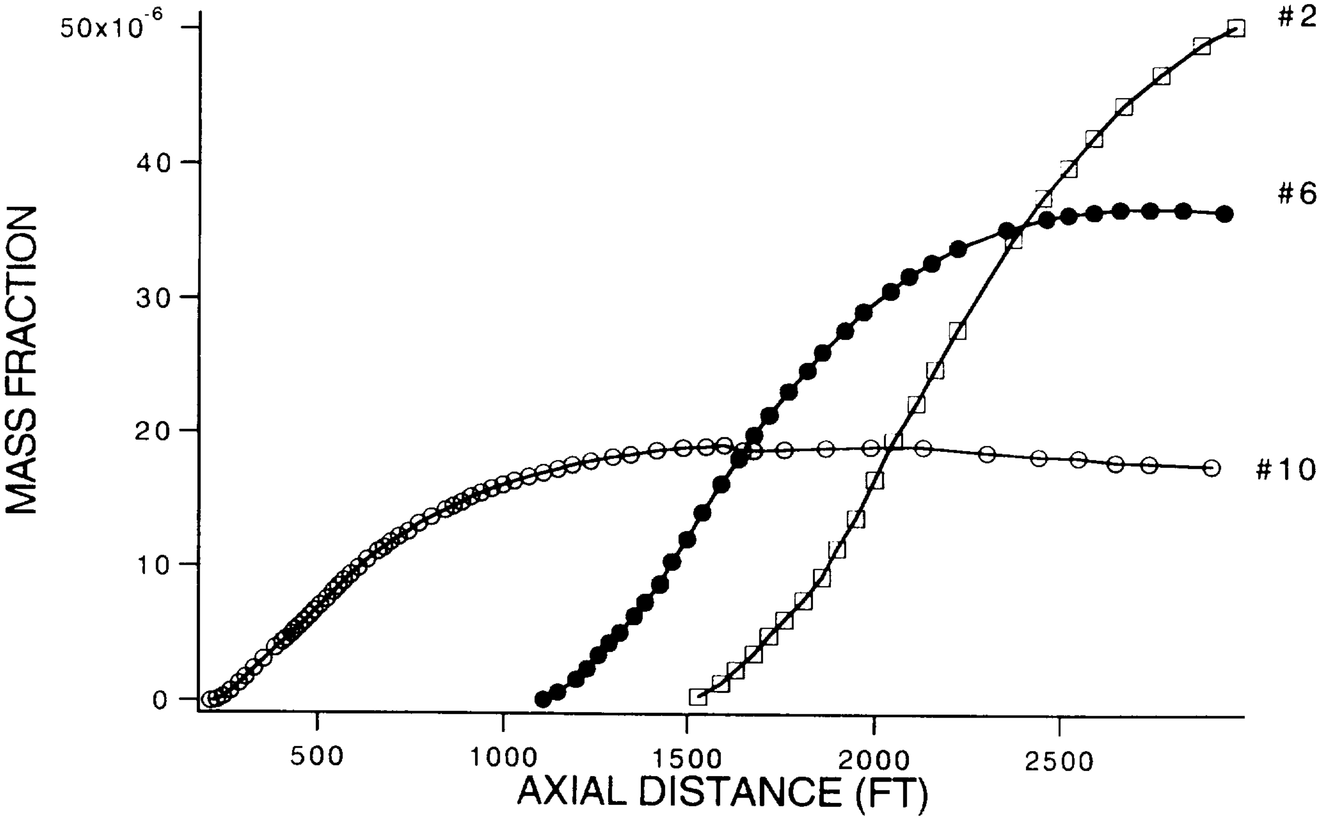

Fig 6: Condensed H_2O mass fraction as a function of plume axial distrance for an exhaust particulate distribution which has been shifted to smaller radii. Results are shown for contrail droplet growth along three different flowfield stramlines (#2 - near plume axis; # 6 - midway between plume axis and plume/ambient boundary; # 10 - near plume ambient boundary).

depends only on the local gas environment, the onset of condensation for each streamline is independent of the exhaust particulate number density or size distribution. The profiles also illustrate that the mass fraction of condensate increases towards the plume axis due to the increased water vapor mass fraction in this region.

The mass fraction of water vapor which condenses is also sensitive to the exhaust particulate number density and size distribution. Comparing the profiles in Figure 4 to those in Figure 5, it can be seen that reducing the number of activated CN by two orders of magnitude reduces the mass fraction of condensed H_2O by approximately the same factor. A similar effect is seen in Figure 6. In this case, the exhaust particulate mass loading is the same as in Figure 4, but the size distribution is shifted to smaller diameters. This increases the CN number density and, consequently, reduces the mass fraction of condensate.

Figure 7 shows the fraction of H_2O which has condensed as a function of axial distance for the two exhaust particulate distributions in Figure 3. For each distribution, profiles are shown assuming 100% and 1% of the soot particles are activated. These results further illustrate the general trends seen in Figures 4-6. In addition, they indicate that less than 25% of the available water has condensed within 3000 ft of the exit plane, even when 100% of the soot particulates are activated.

The CN number density and size distribution also affects the size distribution of contrail droplets. This is illustrated in Figures 8 and 9 which display the ratio of the contrail droplet radius, r_d, to the core nuclei radius, r_c, as a function of r_c for condensation along streamline #6. At the saturation point (time=t_s) this ratio is unity since there has been no condensation. At later times, $t > t_s$, the ratio r_d/r_c increases as condensation proceeds. For a fixed time, $t-t_s$, the relative growth indicated by this ratio depends on the exhaust CN number density and size distribution (i.e. r_c).

Figure 8, for example, illustrates the affect of changes in the CN number density. Results are shown for $t-t_s$ equal to 0.4 sec and 0.85 sec. The shaded histogram depicts contrail droplet growth for the base exhaust CN distribution (see Figure 5), while the unshaded histogram shows the relative growth for the same size distribution, but with the exhaust particulate mass loading reduced two orders of magnitude. Within the limitations of the current model, this is equivalent to assuming that only 1% of the exhaust particulates described by the base distribution are activated. It can be seen that while a decrease in the activated CN number density decreases the mass fraction of vapor which condenses (cf. Figures 4 and 5) individual droplets tend to grow larger. As shown in Figure 8, this effect is greater for smaller droplets.

Figure 9 illustrates the effect of shifting the CN size distribution on the relative droplet growth by showing the ratio r_d/r_c versus r_c for the two CN distributions in Figure 5. The unshaded histogram in Figure 8 depicts the relative droplet growth for the base distribution in Figure 5, while the shaded histogram shows the relative growth that results when the CN distribution is shifted to smaller radii at a constant mass loading. These results are consistent with those shown in Figure 8. Thus, for a constant exhaust particulate mass loading, shifting the CN distribution to smaller radii results in an increase in the CN number density and, correspondingly, a decrease in the size of contrail droplets that result from condensation over a given length of time.

Nitric Acid Condensation

Nitric acid condensation was treated using the kinetic condensation model. However, the model predicted a negligible effect on contrail droplet sizes due to the low levels of nitric acid in the plume. The nitric acid mole fractions at 500 ft, 1011 ft and 1520 ft downstream of the exit plane were 2.0×10^{-7}, 9.5×10^{-8} and 6.6×10^{-8}, respectively. These levels are several orders of magnitude

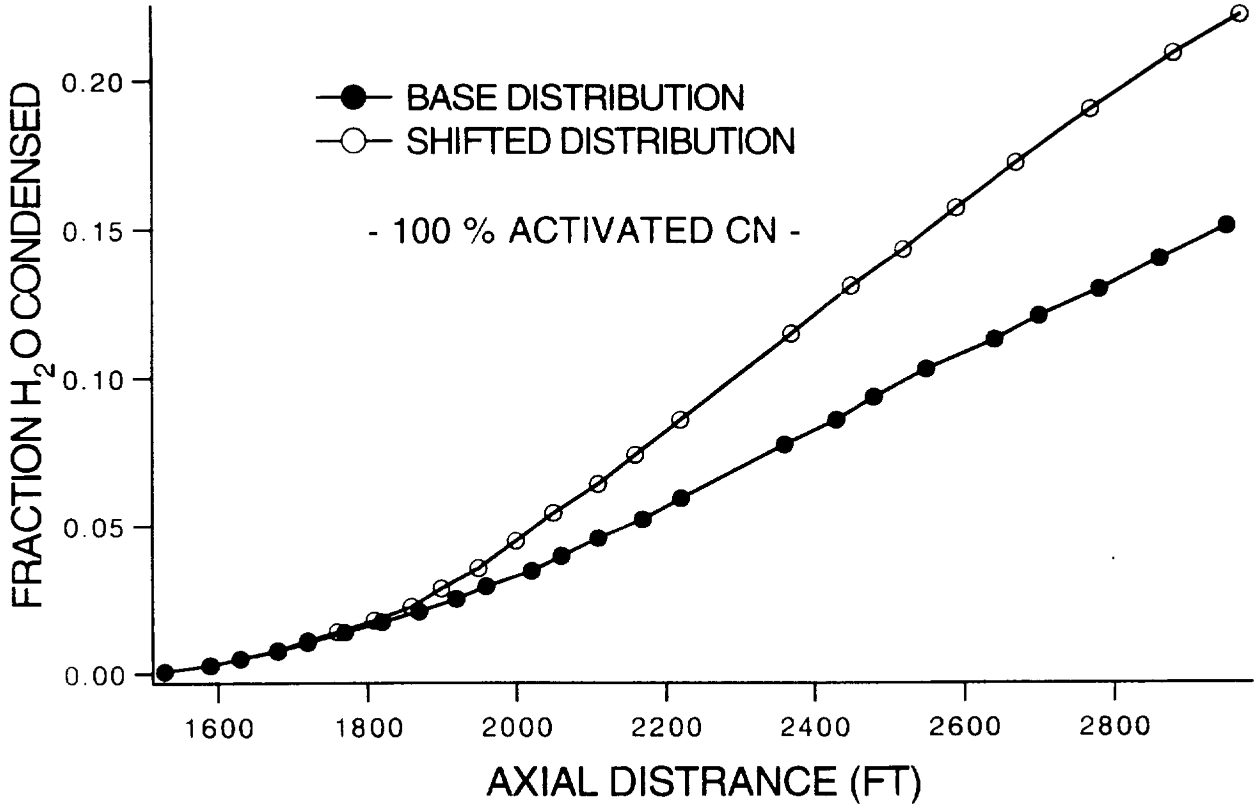

Fig. 7: Fraction of H_2O which has condensed as a function of axial distance. Profiles are shown for two different distributions of exhaust soot. Distribution 1 corresponds to the base distribution. Distribution 2 assumes the same exhaust particulate mas fraction, but is shifted to smaller radii. For each distribution, profiles are shown assuming 100% and 1% of the soot particulates are activated.

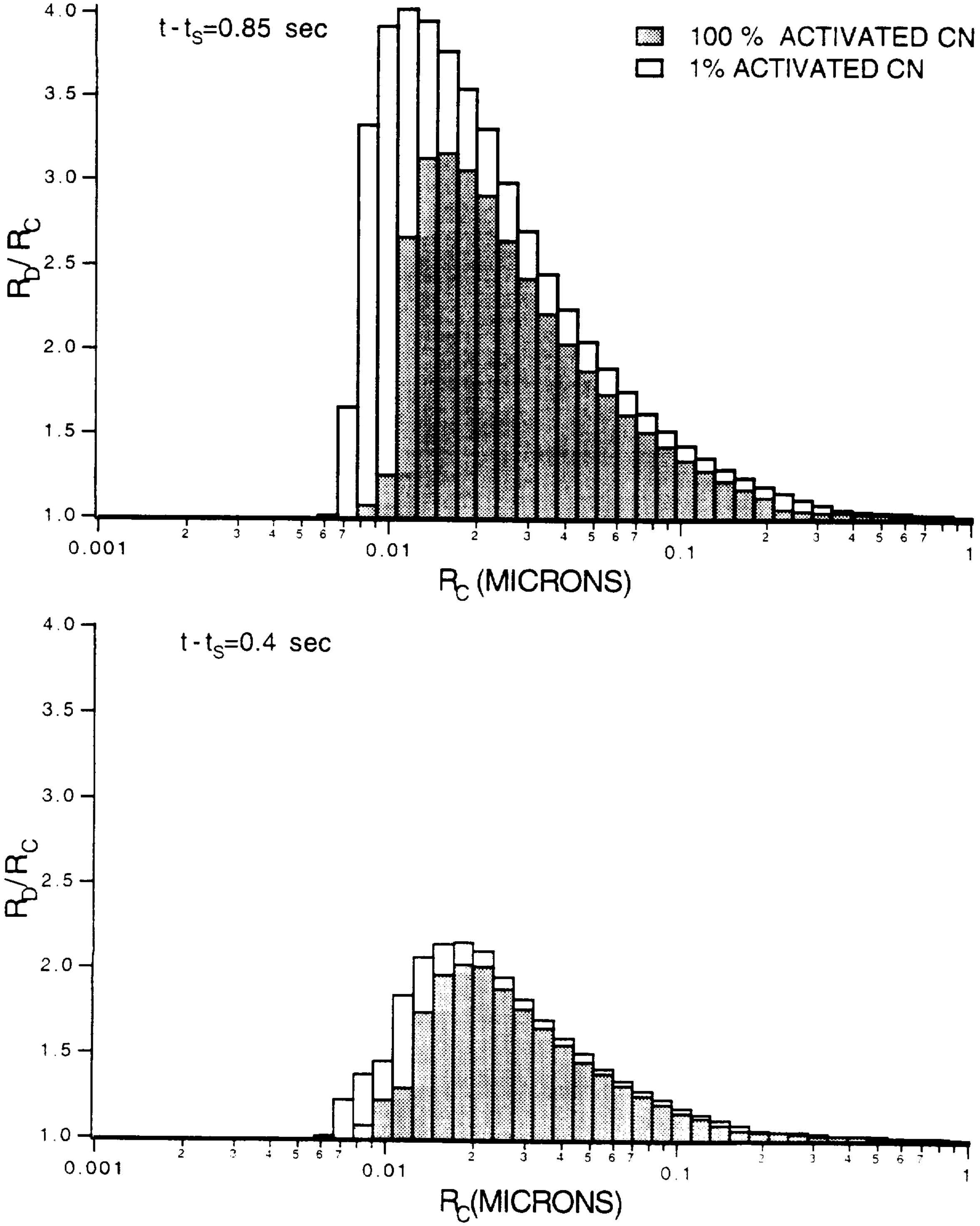

Fig. 8: Effect of activated CN number density on contrail droplet growth. Contrail droplet growth is compared for the base exhaust particulate distribution assuming 100% (shaded histogram) and 1% (unshaded histogram) of the exhaust particles are activated condensation nuclei. r_d is the droplet radius at time t; r_c is the initial core nuclei radius. Results are shown for: (a) $t-t_s=0.4$ and (b) $t-t_s=0.85$, where t_s is the time at which saturation is reached.

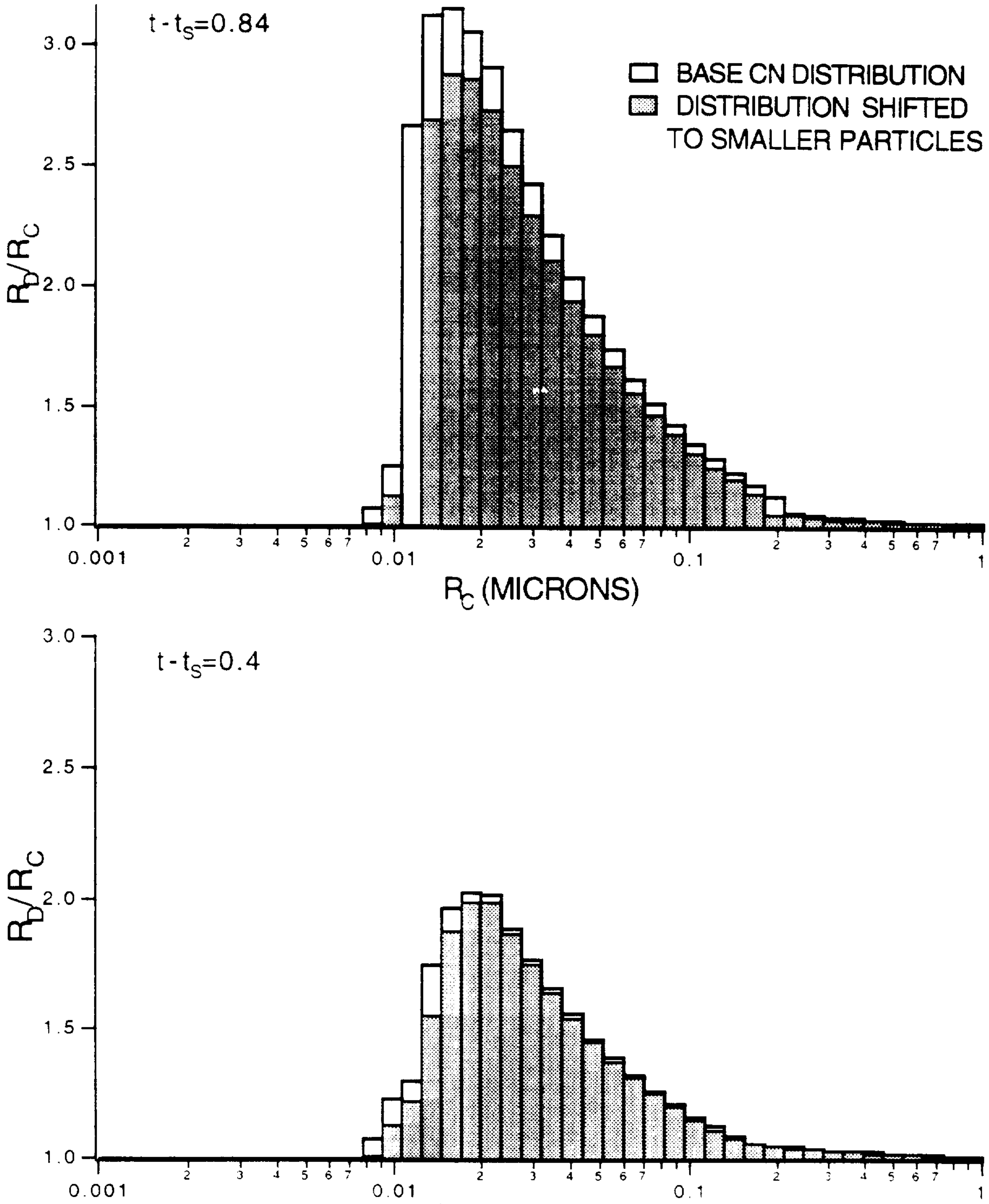

Fig. 9: Effect of activated CN size distribution on contrail droplet growth. Contrail droplet growth is compared for the base exhaust particulate distribution (unshaded histogram) and a distribution with the same exhaust particulate mass fraction, but which is shifted to smaller radii (shaded histogram). r_d is the droplet radius at time t; r_c is the initial core nuclei radius. Results are shown for: (a) $t-t_s=0.4$ and (b) $t-t_s=0.85$, where t_s is the time at which saturation is reached.

too low to significanly affect the condensation kinetics. Although sulfuric acid condensation was not explicitly treated, similar results are expected since the predicted levels (mole fraction) of sulfuric acid are on the order of 10^{-11}.

SUMMARY

The kinetic condensation model developed by Hoshizaki, et. al.[7,8] has been implemented as an overlay on the Standard Plume Flowfield (SPF-2) model to predict heterogeneous condensation for a High Speed Civil Transport flying in the lower stratosphere. Simulations were performed to illustrate the parametric dependence of contrail droplet growth on the exhaust condensation nuclei number density and size distribution. These calculations were performed assuming that insoluble soot particles were the dominant exhaust CN. Model results indicate that the condensation of water vapor is strongly dependent of the number density of activated CN. Based on the experimental results of Hallett et. al.[10] the model results suggest the condensation of soot particulates may not be the primary mechanism driving water condensation in the near field plume.

ACKNOWLEDGEMENTS

The authors acknowledge the support of the NASA High Speed Research Program (HSRP) Atmospheric Effects of Stratospheric Aircraft Project through contract NAS1-19161.

REFERENCES

1. Tuck, A.F, Watson, R.T, Condon, E.P, Margitan, J.J. and Toon, O.B., "The Planning and Execution of ER-2 and DC-98 Aircraft Flights Over Antarctica, August and September 1987," J. Geophys. Res. 94, 11181-1122 (1988).

2. Stolarski, et. al., "Total Ozone Trends Deduced from Nimbus 7 TOMS Data," Geophys. Res. Letters 18, 1015-1018 (1981).

3. WMO, Report of the International Ozone Trends Panel: 1988, World Meteorological Organization, Global Ozone Research and Monitoring Project - Report No. 18, 1988.

4. Weisenstein, D.K., Ko, M.K.W., Rodriquez, J.M. and Sze, N., "Impact of Heterogeneous Chemistry and Model-Calculated Ozone Change Due to High Speed Civil Transport Aircraft," Geophy. Res. Lett. 18, 1991 (1991).

5. Johnston, H.S., Prather, J.J. and Watson, R.T., "The Atmospheric Effects of Stratospheric Aircraft: A Topical Review," NASA Ref. Publ, 1250, January 1991.

6. Miake-Lye, R.C., Martinez-Sanches, M., Brown, R.C., and Kolb , C.E., "plume and Wake Dynamics, Mixing and Chemistry Behind an HSCT Aircraft," AIAA Paper No. 91-3158.

7. Hoshizaki, M., Chou, Y.S., Meyer, J.W., WIlson, K.D. and Thosmas, P.D., "Plume Visibility Detection Study: Volume 1. Tecxhnical Analysis," Report AFRPL-TR-78-32, Lockhjeed Palo Alto Research Laboratgory, Palo Alto, CA, November, 1978.

8. Meyer, J.W., "Kinetic Model for Aerozol Formation in Rocket Contrails," AIAA J. 17, 135 (1979).

9. Fukuta, N. and Walter, L.A., "kinetics of Hydrometeor Growth from as Vapor-Spherical Model," J. Atm. Sci. 27, 1160 (1970).

10. Dash. S.M., Pergament, H.S., Wolf, D.E., Sinha, N., Taylor, M.W., and Vaughn, M.E. Jr. "The JANNAF Standardized Plume Flowfield Code Version II (SPF-II), Volume II" SAIC/PR-TR-18-11, July 1990.

11. Hallett, et. al. Aerosol Sci. Technol. 10, 70 (1989).

12. Appleman, H.S., "The Formation of Exhaust Condensation Trails by Jet Aircraft," Bull. Amer. Met. Soc., Vol. 34, January 1953, pp. 14-20.

13. Miake-Lye, R.C., Matulaitis, J.A., Krauss, F.H., Dodds, W.J., Albers, M., Hourmouziadis, J., Hasel, K.L., Lohmann, R.P., Strander, C., Gerstle, J.H. and Hamilton, G.L., "High-Speed Civil Transport Aircraft Emissions," in The Atomspheric Effects of Stratospheric Aircraft: A First Program Report, NASA Reference Publication 1272, National Aeronautics and Space Adminsitration, 1992.

14. "1990 Conditions Atomspheric Chemistry Data," Atmospheric and Environmental Research, personal communication, 1990.

15. Low, H.C., Scott, C.J. and Veninger, A., "Correlated Fuel Property Effects on an F402-RR-406A (Pegasus) Engine Combustor," presented at the Gas Turbine and Aeroengine Congress and Exposition, Brussels, Belgium, June 11-14, 1990.

16. Rosen, J.M. and Greegor, R., "Jet Engine Sot Emision Measured at Altitude," J. Aircraft 11, 243 (1974).

17. Hofman, D.J. and Rosen, J.M. "Balloon Oservations of a Paritcle Layer injected by a Straospheric Aircraft at 23 Km," Geophsy. Res. Letts. 5, 511-514 (1978).

18. Koch, R., Witig., S., Feld, H.J. and Mohr, H.R., "In Situ Soot Measurements in an Ooeration Engine Gas Turbine Combustor," pesented at the Gas Turbine and Aeroengine Congress and Exposition, Orlando, FL, June 3-6, 1991.

19. Pitchford, M., Hudson, J.G. and Hallett, J., "Size and Critical Suersaturation for Condensation of Jet Engine Exhaust Particles," J. Geo. Res. 98, 787 (1991).

20. Knollenberg, R.C., "Measurement of the Growth of the Ice Budget in a Persisting Contrail, ", J. Atm. Sci. 29, 497-1374 (1972).

Chapter 2

SUBSIDENCE OF AIRCRAFT ENGINE EXHAUST IN THE STRATOSPHERE

INTRODUCTION

The possibility of ozone depletion in the stratosphere caused by oxides of nitrogen (NO_x) in the engine emissions of a projected fleet of high speed civil transports (HSCT) has been a main concern in determining the environmental acceptability of these aircraft. The amount of ozone destroyed by the engine emission depends on both the amount of emitted NO_x and its residence time in the stratosphere. Reduction of engine emissions is the subject of intense research by engineers in aircraft engine companies and in NASA's combustion research laboratories. The residence time of NO_x in the lower stratosphere is very sensitive to the location of the deposition altitude relative to the tropopause. If the deposition altitude is close to the tropopause, the engine emissions are easily transported to the troposphere, thus potentially reducing the ozone destruction.

All current two-dimensional assessment studies of the atmospheric impact of HSCT emissions assume that the altitude of deposition of NO_x corresponds to the altitude of the flight corridor. However, different mechanisms could alter this approximation. For example, convective oscillations during the early wake regime could lead to adjustments of the deposition altitude (Miake-Lye et al., 1993; Overcamp and Fay 1973). The enhancement of water and reductions of ozone in the wake relative to the surrounding atmosphere could result in differential radiative cooling and parcel sinking. An early study by estimated a subsidence velocity of about 0.06-0.3 km/day in the lower stratosphere; if such velocities were maintained for several days, the exhaust parcel could sink by 1 km or more, thus reducing its potential for ozone depletion.

This study reassesses the significance of net radiative cooling of exhaust parcels in determining the deposition altitude of NO_x, and its potential impact on calculated ozone reductions by HSCTs. Several factors justify such a reevaluation. In the first place, updated information on emission indices for water and NO_x appropriate for HSCTs are incorporated. Secondly, an updated model for the jet and vortex regimes of the exhaust plume is used to place constraints on the dilution of radiatively and chemically active species between the exit plane and the beginning of the far-wake regime (i.e., after breakdown of the vortex pairs). A Lagrangian box model with up-to-date chemistry and parameterized, scale-dependent diffusion is used to calculate the time-dependent behavior of radiatively active species, mainly water and ozone. These calculations are then incorporated into a radiative transfer model to calculate the differential cooling rates and subsidence velocities.

Section 2 contains a brief description of our choice of initial conditions and the Lagrangian box model used. The radiative transfer code and the differential heating rates calculated by this code are discussed in section 3, and used to derive subsidence velocities. General conclusions are presented in section 4.

LAGRANGIAN BOX MODEL

a) Scale-dependent mixing

The Lagrangian box model solves an equation of the form (Gelinas and Walton, 1974):

$$\frac{dn_i(t)}{dt} = P_i - L_i - \left(\frac{d\ln V(t)}{dt}\right)\left[n_i(t) - n_i^a(t)\right] + R_i(t) \tag{1}$$

where P_i and L_i denote the chemical production and loss for species i, n_i and $n_i^a(t)$ represent the concentrations of species i within the plume and in the background atmosphere, respectively, and R_i denotes other production/loss processes, such as, for example, denitrification. The factor $d\ln V(t)/dt$ represents the entrainment parameter, where the volume V(t) is defined as that physical volume which contains all the initial plume molecules.

We have implemented a scale-dependent dispersion, following the formalism of Gelinas and Walton (1974). In this formalism, the wake is treated as a Gaussian plume, and its time-dependent volume V(t) is assume to expand according to the expression:

$$\frac{d\ln V(t)}{dt} = \frac{K_y}{\sigma_y^2} + \frac{K_z}{\sigma_z^2} \tag{2}$$

In (2), the vertical and horizontal dimensions σ_z, σ_y are given by the equations:

$$\frac{d\sigma_y^2}{dt} = 2K_y(t) \tag{3}$$

$$\frac{d\sigma_z^2}{dt} = 2K_z(t)$$

The horizontal and vertical eddy coefficients K_y, K_z can be assumed constant, or be related to the dimensions by expressions consistent with similarity theory. In particular, Gelinas and Walton suggest the expression:

$$K_{y,z} = \left(\frac{1}{b\varepsilon^{1/3}\,\sigma_{y,z}^{4/3}} + \frac{1}{K_{y,z,m}}\right)^{-1} \tag{4}$$

where b is a constant of order 1, ε the energy dissipation rate, and $K_{y,z,m}$ an asymptotic value for the eddy coefficient appropriate for large wake sizes.

It is difficult to obtain reliable estimates for the parameters in equation (4). The large-scale distribution of trace gases in the stratosphere can be obtained with horizontal "eddy" coefficients of order 10^9 - 10^{10} cm^2s^{-1} (Ko et al., 1985). At the same time, the length scale of the eddies responsible for these processes is much larger than that acting on aircraft wakes. Arguments from similarity theory suggest that horizontal eddy coefficients should be about as much as factor of 10^4 smaller for scales less than 1 km (Overcamp and Fay, 1973). Vertical eddy coefficients in the lower stratosphere are of order 10^3 cm^2s^{-1}, and are expected to be maintained by small-scale processes. There is virtually no information on the energy dissipation parameter ε.

We carried out calculations of the time-development of aircraft wakes for a period of 5 days with the following assumptions for the mixing:

i) No mixing.

ii) $K_{ym} = 10^3 cm^2 s^{-1}$, $\varepsilon = 2 x 10^{-2} cm^2 s^{-3}$ (Gelinas and Walton, 1974) $K_{zm} = 10^3 cm^2 s^{-1}$.

iii) As above, but with $K_{ym} = 10^4 cm^2 s^{-1}$.

Consideration of equation (4) indicates that the adopted large-scale diffusion coefficient $K_{y,z,m}$ will dominate the mixing over most of the wake regime. The above choices for cases are biased towards rather small mixing coefficients; faster mixing would imply complete dissipation of the plume in periods much less than a day, with negligible sinking. Since heterogeneous chemistry on contrails is not expected to occur over several days, we did not include heterogeneous processes in this set of calculations. Background conditions are adopted from 2-D model results at 47°N, 17.8 km, summer, which assume heterogeneous chemistry on background aerosol particles (Rodriguez et al., 1991; Weisenstein et al., 1992).

b) Initial conditions

The model described above is applicable to the far-wake regime, ie., after breakdown of the vortex pair. Dynamical simulations (Miake-Lye et al., 1993) of the jet and vortex regimes suggest a dilution factor of about 1100 between the exit plane and the beginning of the vortex regime, for chemically inert species. Such dilution factors are applied to water. For chemically active species, such as nitrogen oxides, we would ideally need to incorporate full chemistry in both the jet and vortex regimes. These calculations have been carried out in the jet regime by the Aerodyne, Inc. group (Miake-Lye et al., 1993), but no calculations are available for the vortex regime. We thus assume that the NO_x concentrations are approximately given by simple dilution of the exit plane values. Ozone concentrations are initialized with the background atmosphere values, since calculations do not indicate significant ozone production/removal during the first hour of the wake.

Estimates for the air flow range from 100 - 200 kg/s per engine, for aircraft flying at Mach 2.4 at 17.8 km. Assuming an emission index of 1000 g H_2O/kg fuel, and 15 g NO_x/kg of fuel, we estimate initial concentrations in the wake regime ranging from 27.5 to 55.0 ppmv for H_2O, and 43.5 to 87.0 ppbv for NO_x. These represent enhancements of factors of 6.5 to 13 for water, and over two orders of magnitude for NO_x, relative to calculated values in the surrounding atmosphere.

Our calculations also require specification of the initial plume sizes $s_{y,z}$ to be used in equations (1) - (4). Calculations by Miake-Lye et al. (1993) suggest linear dimensions of about 70 m after vortex breakdown. We have thus adopted $\sigma_{zo} = \sigma_{yo} = 70$ m.

c) Results

We have used the coupled equations (2)-(4) to solve for the time-dependent increase for vertical and horizontal dimensions of the wake. Calculated values for σ_y are shown in Fig. 1, for $K_{y,m} = 10^3$ and $10^4 cm^2 s^{-1}$. Values for σ_z are identical to those of σ_y for the $K_{y,m} = 10^3 cm^2 s^{-1}$ case. In the limiting case with no mixing, the horizontal and vertical dimensions would stay constant for the assumed length of the calculation.

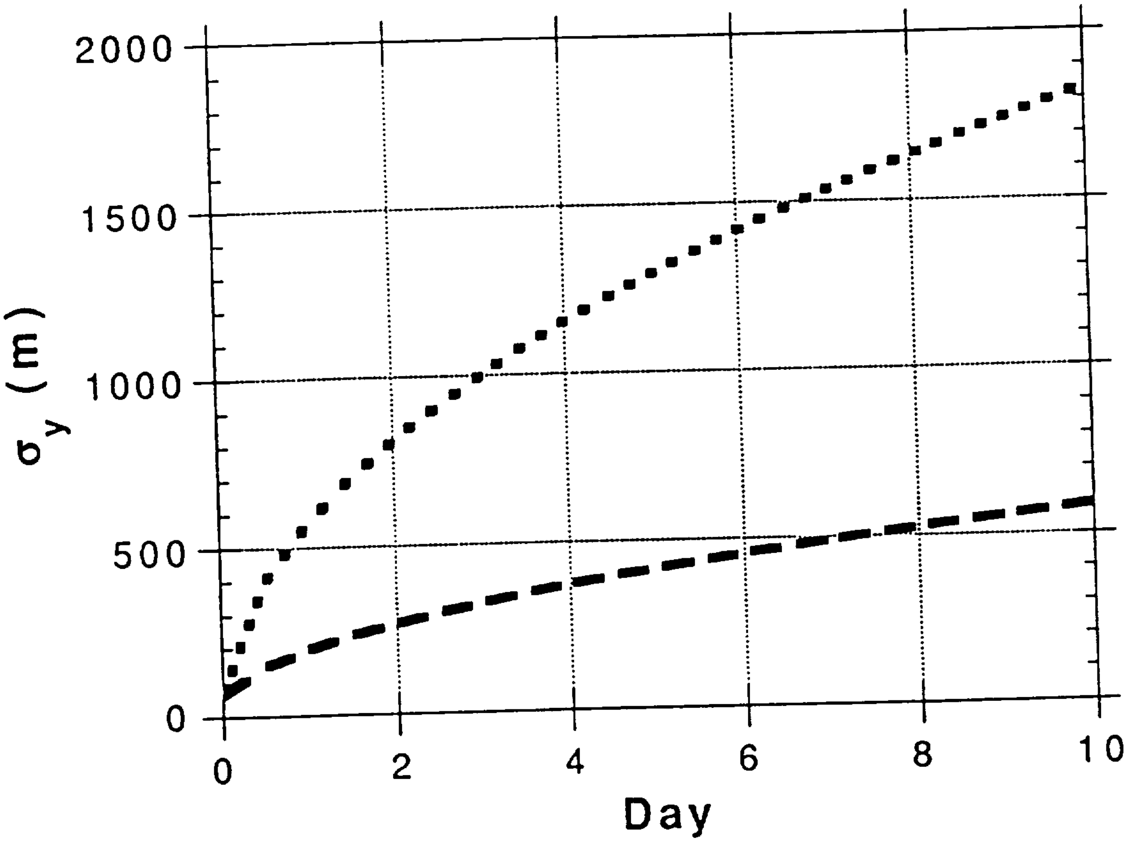

Fig. 1: Calculated increase in the horizontal dimension σ_y. We adopt the formulation in equations 1-4. The dotted line adopts a value of $K_{ym} = 10^4$ cm^2 s^{-1}, while the dashed line assumes a value of $K_{ym} = 10^3$ cm^2 s^{-1}. See text for details.

Examination of Fig. 1 suggests that, for the assumed mixing parameters, the vertical dimension would increase by about a factor of two in the first day of the wake regime. The horizontal dimension could increase by factors of 2-5. We would thus expect decreases in the water concentration of factors of 5 - 10 over the first day. Such decreases are confirmed in the time-dependent calculations of water illustrated in Fig. 2a. Water in the wake decreases to near background values (4.2 ppmv for these conditions) in 1-2 days for the cases which assume mixing. Similar decreases are calculated for NO_x concentrations (not shown).

The calculated concentrations of ozone are shown in Fig. 2b. Except for the limiting case of no mixing, the calculated decrease in ozone due to enhanced NO_x in the wake is negligible. In the case of no mixing, ozone would decrease by about 1%/day within the wake. As discussed below, such ozone reductions will be unimportant in determining the radiative behavior of the wake.

We stress that the above results incorporate the latest estimates received from Aerodyne scientists on dilution rates and plume sizes, and thus supersede previous calculations presented in our previous interim annual reports.

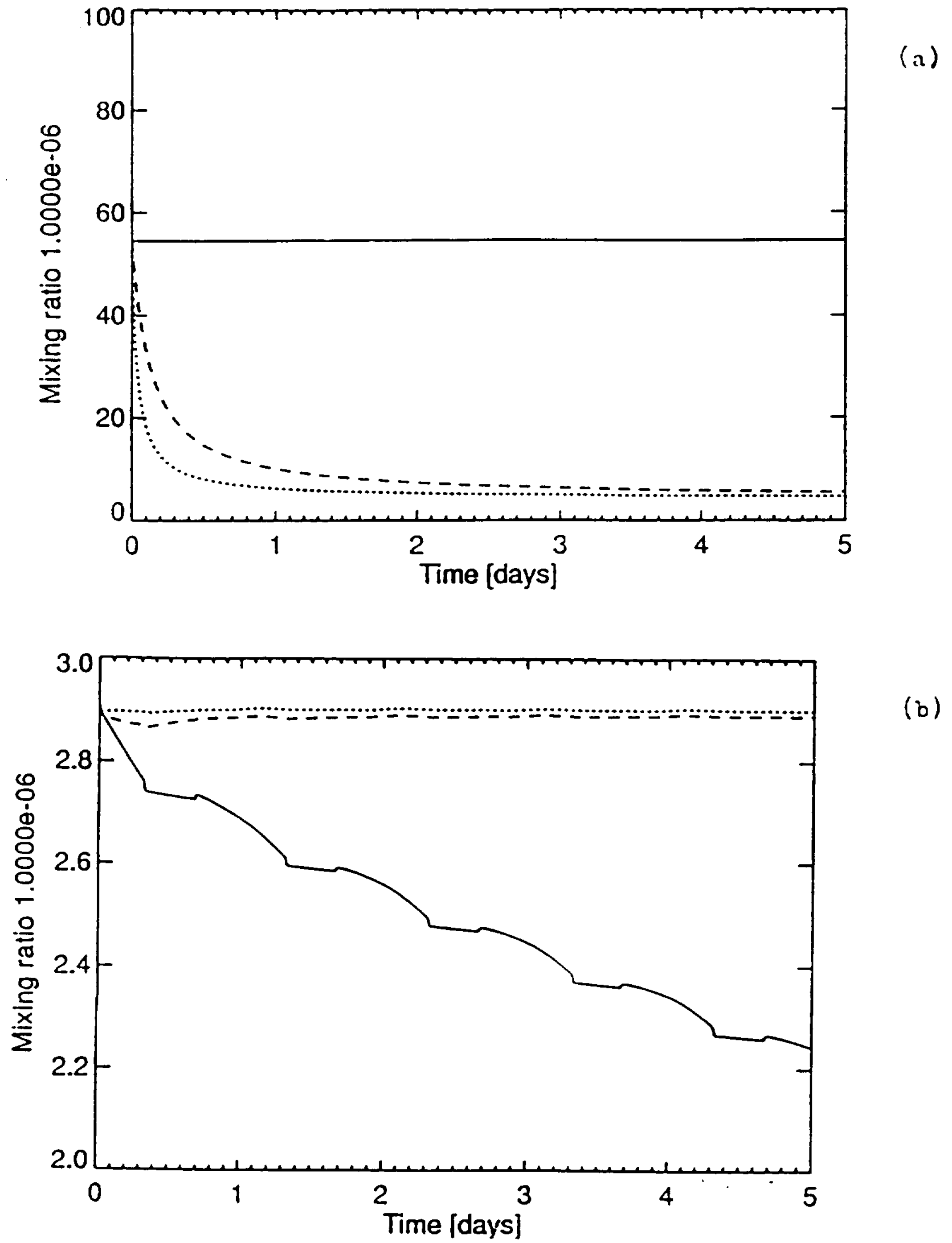

Fig. 2: Calculated concentrations of water (panel a) and ozone (panel b). Initial conditions assume an upper limit for engine air flow and dilution factors from exit plane to the far wake (see text for details). Results denoted by solid lines assume no mixing. The dashed and dotted line correspond to the same assumptions for mixing as in Fig. 1.

DIFFERENTIAL COOLING RATES AND SUBSIDENCE VELOCITIES

a) Radiative heating/cooling calculations

The difference of the abundance in radiatively active tracer gases, e.g. lower ozone, higher water vapor, and higher CO_2, between the aircraft wake and the background atmosphere all lead to differential cooling of the wake relative to the background. The dilution estimates discussed above indicate that CO_2 concentrations will have diluted to background values by the beginning of the wake regime. Radiative effects will therefore be induced by water and maybe ozone.

Differential radiative heating rates have been calculated using a one-dimensional plane-parallel radiative transfer model for a inhomogeneous atmosphere with vertical resolution of 3.5 km (Lacis and Hansen, 1974, Wang and Ryan, 1983). The model has been modified to include an extra layer of 70 m thickness at different altitudes, to simulate an aircraft wake. Solar heating rates are calculated based on the parameterization of Lacis and Hansen (1974). The absorption by H_2O, CO_2, O_3, NO_2 and O_2 and the multiple scattering by all atmospheric molecules (i.e. the Rayleigh scattering) are calculated using the adding method. The thermal (infrared or IR) heating rates are calculated using the Malkmus narrow band model with 27 spectral intervals. The gases included in the thermal heating calculation are H_2O, CO_2, O_3, N_2O, CH_4, NO_2, CFC-11 and CFC-12. This model has been incorporated into the AER two-dimensional, interactive model to calculate self-consistent background radiation and ozone fields in the stratosphere for present-day conditions (Ko et al., 1993). Background concentrations of water and other species are also taken from the 2-D model.

Because of the change of radiation field with altitude, the differential cooling rate will be altitude dependent. Furthermore, calculations of the time-dependent behavior of water and ozone at different altitudes would have to include both the vortex dynamics, chemistry and mixing appropriate to those altitudes. Given the large uncertainty in the mixing parameterizations in the model, we have instead normalized the concentrations of water and ozone shown in Fig. 2 to the background values at that altitude, and assumed the same relative enhancement in water and reduction in ozone for all latitudes and seasons, and for altitudes ranging from 13 to 25 km. Radiative calculations are carried out once a day for a period of 7 days of maximum plume lifetime.

The different components of the calculated differential radiative heating rates are shown in Figs. 3-5 for the first day of the plume, corresponding to our upper limit water enhancement of a factor of 13, for northern winter conditions. The calculated differential heating rate consists of two components: a positive increase in direct solar absorption by water (Fig. 3) of order 1-2 K/day, and a net cooling in the infrared, also by the enhanced water concentrations (Fig. 4), of order 4-5 K/day. Net cooling rates of between 2 and 4 K/day are calculated in the lower stratosphere (Fig. 5), for these conditions. The altitude and latitude distribution of differential heating rates is similar to those in Figs. 3-5 at other times of the year.

In the extreme limit of no mixing, heating rates in Figs. 3-5 will be the same for subsequent days. In the case of mixing, the calculated heating rates will be smaller, due to the rapid decrease in water calculated in Fig. 2. Due to the optical thinness of the wake, the calculated heating/cooling rates are linear with the relative water enhancement. This is shown in Fig. 6, which shows the differential solar heating, cooling, and net cooling calculated for different enhancements of water for winter, 17.8 km, 47 °N conditions. These results thus provide a simple scaling which allow calculation of the heating rates for different scenarios of water enhancement and/or subsequent dilution.

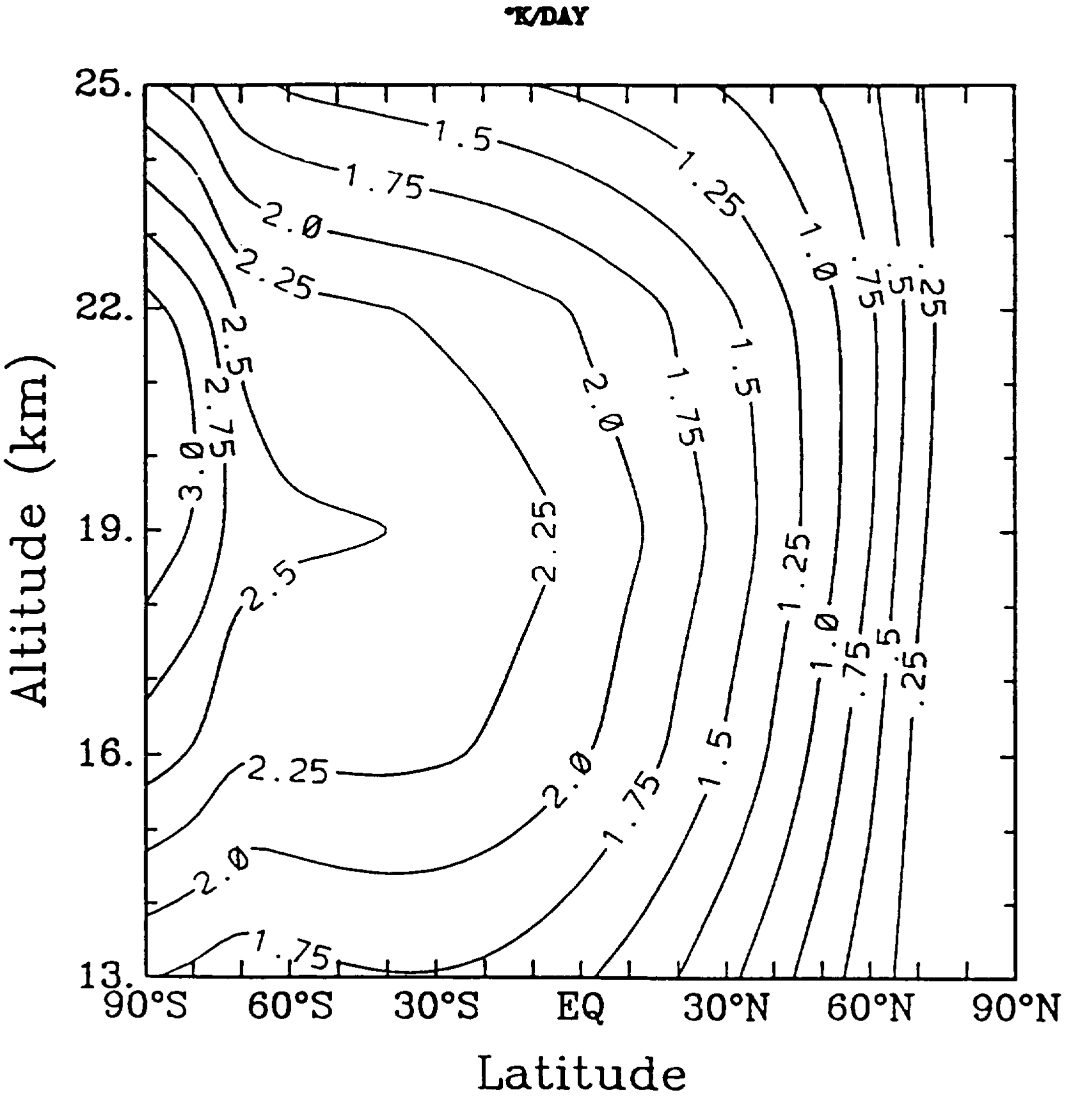

Fig. 3 Differential solar heating rate (°K/day), for Jan. 30 at the beginning of the far wake regime after vortex breakdown. The water vapor is 12.8 times higher than the background. The contour is 0.1 K/day.

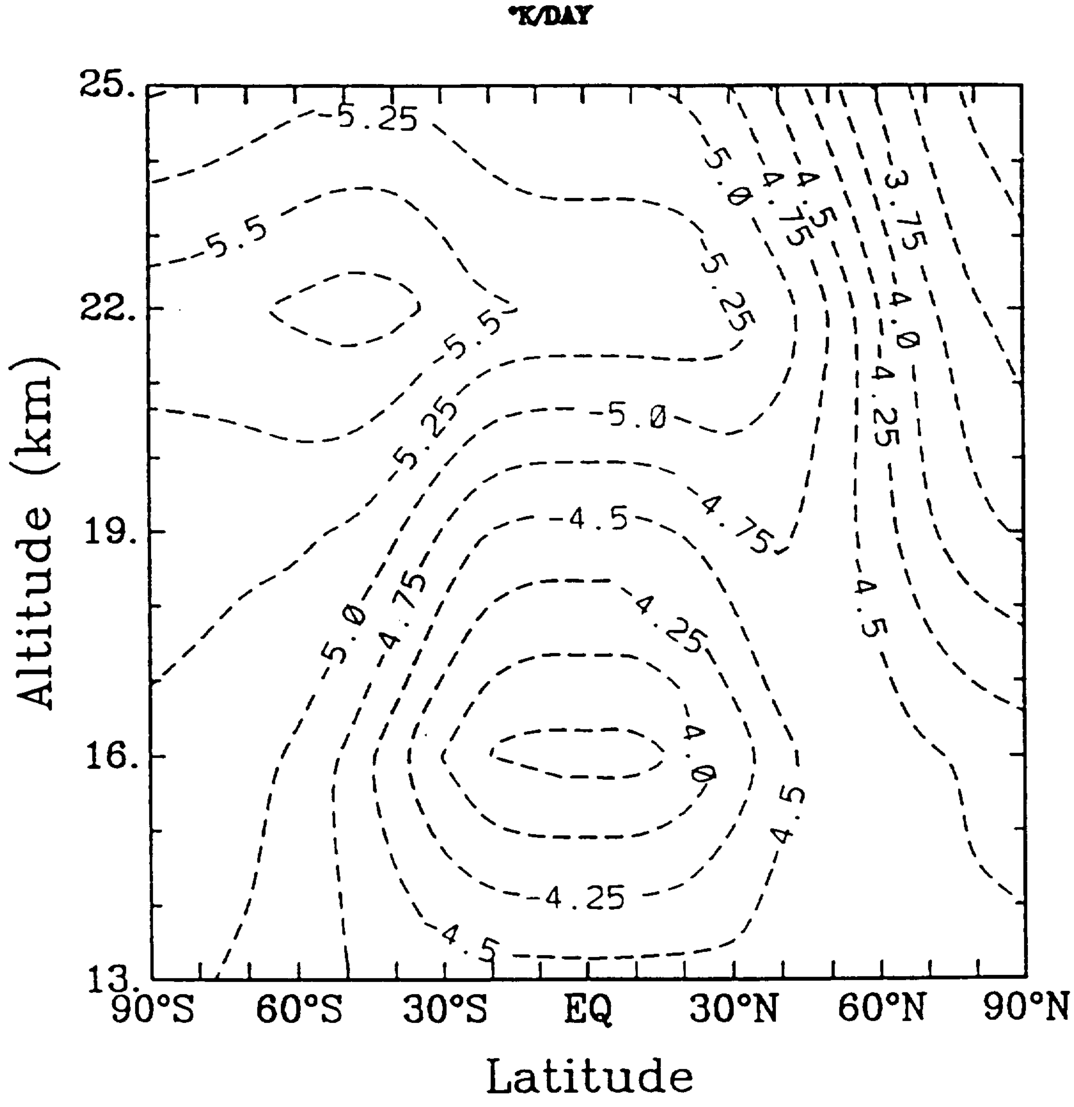

Fig. 4: Same as Fig. 3, but for the infrared cooling rate.

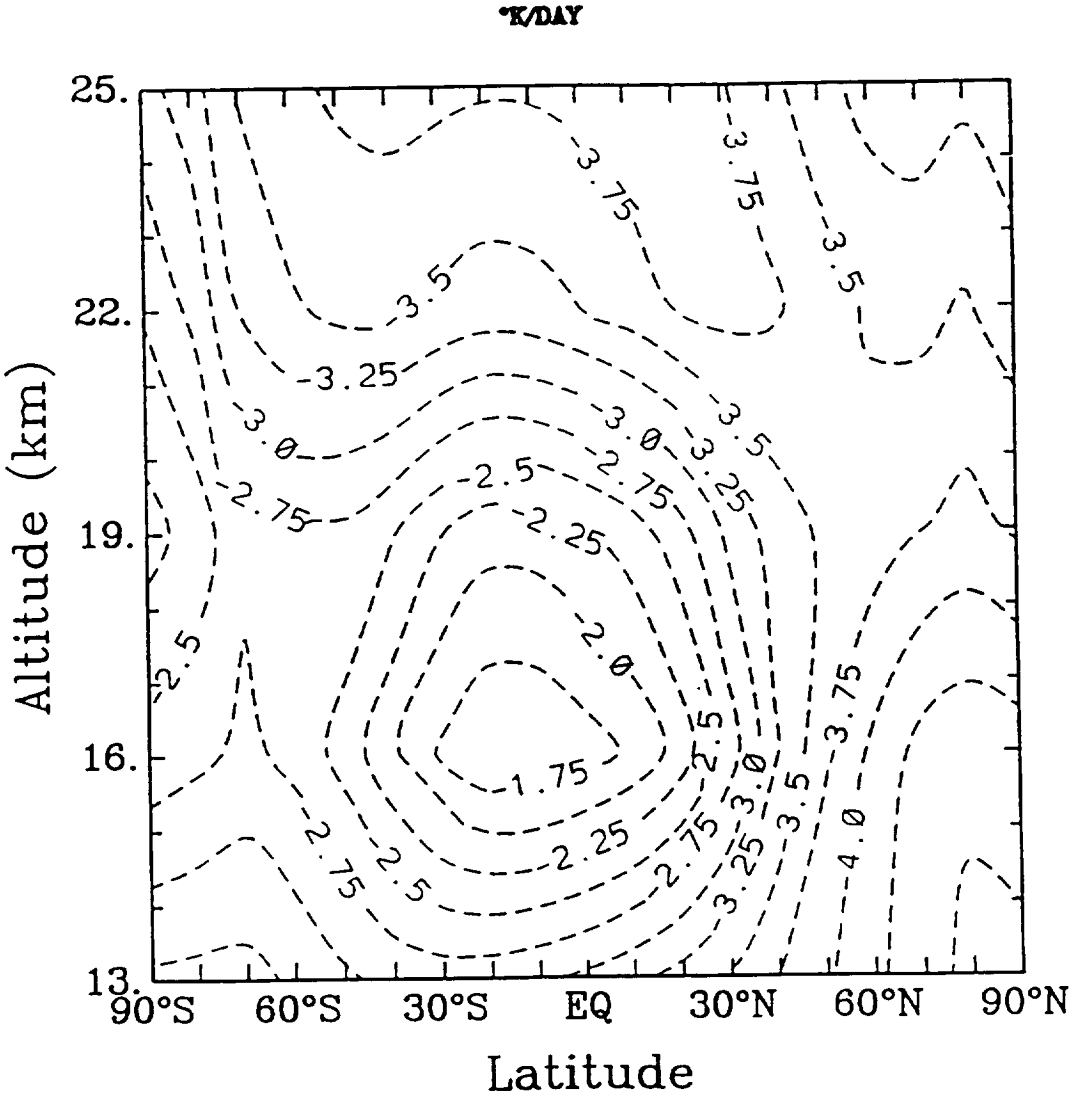

Fig. 5: Same as Fig. 3, but for the net cooling rate.

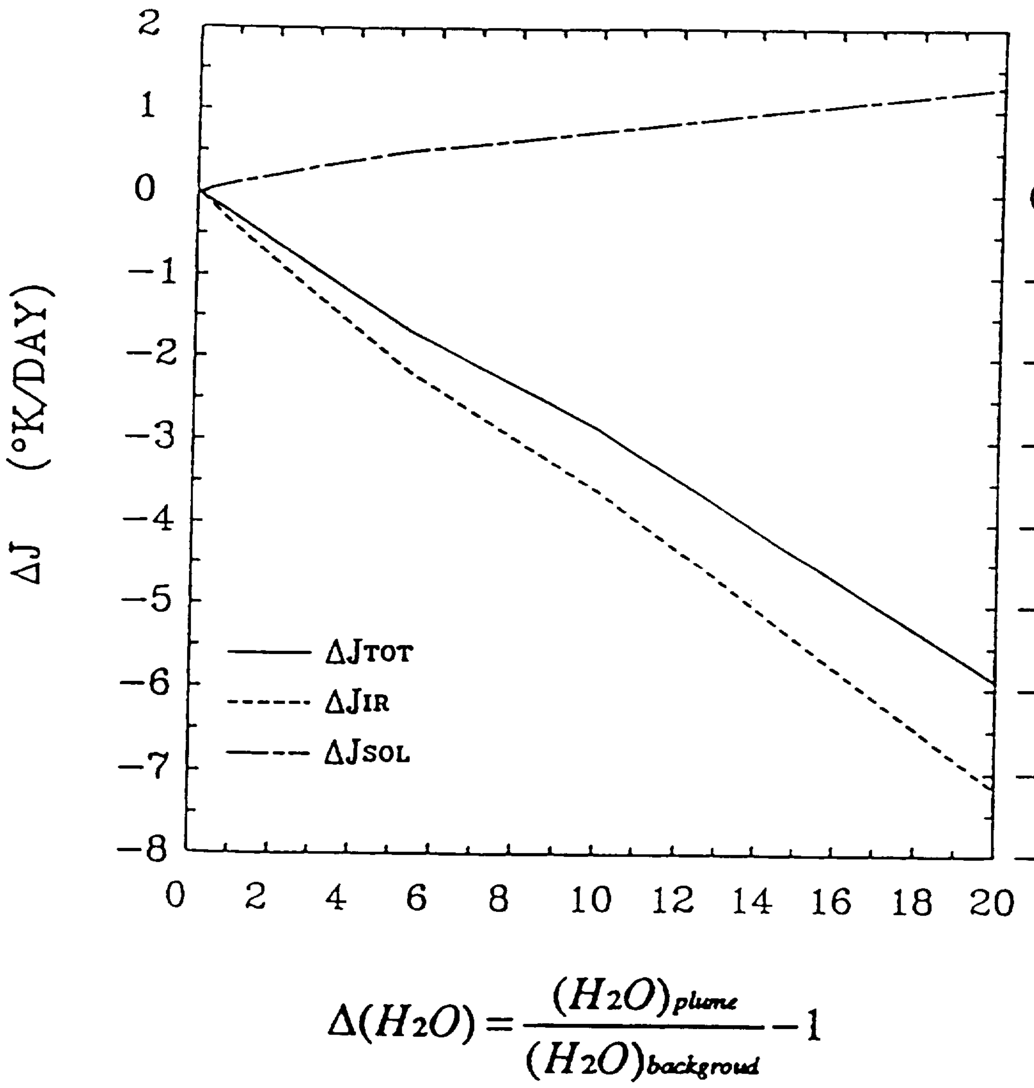

Fig. 6: The net radiative cooling rate (solid line), and its solar heating (dashed line) and infrared cooling (dash-dot line) contributions at 17.8 km, 47°N, Jan. 30 , as a function of the ratio of water vapor.

b) Subsidence of plume

The subsidence velocity w of a parcel of engine exhaust due to the differential net heating rate ΔJ has been derived assuming that the w is such as to maintain the same potential temperature as the surrounding air, (see e.g. Andrew et al., 1987)

$$w = \frac{\Delta J}{\Gamma} \tag{5}$$

where Γ is the stability parameter of the air.

$$\Gamma = \left(\kappa \frac{T}{H} + \frac{\partial T}{\partial Z} \right) \tag{6}$$

where H, the atmospheric scale height, is about 7 km; T is the temperature, Z is the altitude, $\kappa = R_d/C_p = 0.286$, R_d is the gas constant for dry air and C_p is the specific heat at constant pressure. For conditions of the lower stratosphere, the stability parameter Γ has an approximate value of 10 K/km. Subsidence velocities (km/day) can thus be approximated by dividing the heating rates (°K/day) by a factor of 10.

Subsidence velocities of about 0.3 km/day are calculated on the first day of the wake regime. If the initial water concentrations could be maintained for several days, it could lead to substantial sinking of the parcel. However, such conditions are unlikely, and we must consider the mixing cases in Fig. 2. In this case, the heating rates calculated at the beginning of each day can be linearly extrapolated (Fig. 6) to estimate the subsidence velocity as a function of time.

The trajectory of a plume initially at 17.8 km is shown in Fig. 7 for a period of seven days. The results denoted by the dotted line assume that the parcel mixing with the background atmosphere is negligible during this period of time. In this case, the parcel sinks a total of 2.2 km. We stress however, that we consider this result an absolute upper limit for the parcel sinking, since it combines and upper estimate for the initial water concentrations with assumptions of no mixing. A more realistic scenario would be that illustrated by the solid line, which adopts the same initial conditions for water, but assumes the mixing parameterization with $K_{ym} = 10^3$ cm^2 s^{-1}. In this case, the water decreases rapidly, and the parcel sinks only 0.4 km.

CONCLUSIONS

The calculations presented above thus show that the expected sinking in an HSCT plume comes mostly from the effect of enhanced water within the wake. A net sinking of at most 0.4 to about 1 km is estimated for the exhaust parcels after breakdown of the trailing vortex pair. The effect of this subsidence on the calculated ozone impact is small. We also stress that these results represent an upper bound for this estimate, since we have assumed high water emissions and slow mixing of the wake with the surrounding atmosphere.

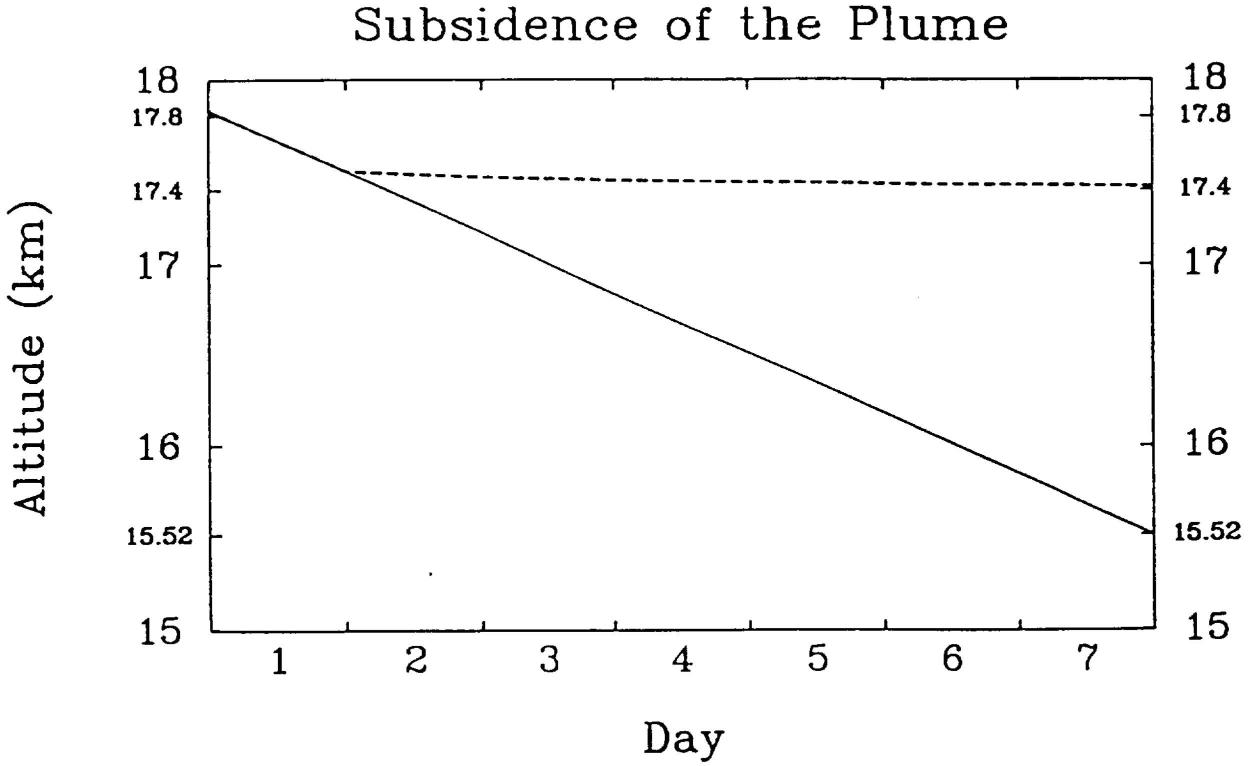

Fig. 7: Total subsidence of a plume, initially at 17.8 km, 47°N, Jan. 30. The solid line assumes no mixing of the parcel, and thus a constant sinking speed of 0.3 km/day, calculated from the results in Fig. 5. The dashed line assumes mixing with $K_{ym} = 10^{3}$ cm^2 s^{-1}, and adopts changing cooling rates corresponding to the decrease in water calculated in Fig. 2a (dashed line).

REFERENCES

1. Andrews, D.G., J.R. Holton, and C.B. Leovy (1987) *Middle Atmosphere Dynamics*, Academic Press, Inc., New York.

2. Gelinas, R.J. and J.J. Walton (1974) Dynamic-kinetic evolution of a single plume of interacting species. *J. Atmos. Sci.*, **31**, 1807.

3. Ko, M.K.W., K.K. Tung, D.K. Weisenstein, and N.D. Sze (1985) A zonal mean model of stratospheric tracer transport in Isentropic coordinates: Numerical simulations for Nitrous Oxide and Nitric Acid. *J. Geophys. Res.*, **90**, 23130-2329.

4. Ko, M.K.W., H.R. Schneider, R.-L. Shia, D.K. Weisenstein, and N.D. Sze (1993) A two-dimensional model with coupled dynamics, radiation and photochemistry. 1: Simulation of the middle atmosphere. Submitted to *J. Geophys. Res.*

5. Lacis, A.A. and J.E. Hansen (1974) A parameterization for the absorption of solar radiation in the earth's atmosphere. *J. Atmos. Sci.*, **31**, P118-133.

6. Miake-Lye, R.C., M. Martinez-Sanchez, R.C. Brown and C.E. Kolb (1993) Plume and wake dynamics, mixing, and chemistry behind an HSCT aircraft. *J. Aircraft*, in press.

7. Overcamp, T.J. and J.A. Fay (1973) Dispersion and subsidence of the exhaust of a supersonic transport in the stratosphere. *J. Aircraft.* **10**, 720-728.

8. Rodriguez, J.M., M.K.W. Ko, and N.D. Sze (1991) Role of heterogeneous conversion of N_2O_5 on sulphate aerosols in global ozone losses. *Nature*, **352**, 134-137.

9. Wang, W.-C., and P.B. Ryan (1983) Overlapping effect of atmospheric H_2O, CO_2 and O_3 on the CO_2 radiative effect. *Tellus*, **35B**, P81-91.

10. Weisenstein, D., M.K.W. Ko and N. D. Sze (1992) The chlorine budget of the present day atmosphere: A modeling study. *J. Geophys. Res.*, **97**, 2547-2559.

Chapter 3

EVALUATION OF SUB-GRID INHOMOGENEITIES IN H_2O AND TOTAL NITROGEN ALONG FLIGHT CORRIDORS

INTRODUCTION

Assessment of the potential impact of exhaust from a proposed fleet of High Speed Civilian Transport (HSCTs) requires understanding of the chemical and dynamical process affecting effluents as they react and mix with the background atmosphere. The study of these mechanisms must consider three regimes (see Fig. 1, and discussion below): 1) modeling of the chemical transformation and dispersion of individual plumes (at scales of order 100's of meters); 2) modeling of the impact of superposition of individual plumes due to repeated flights along a "flight corridor", where a flight corridor is loosely defined as that area containing individual flight plumes before mixing into the background atmosphere (scale of 100's of km); 3) incorporation of exhaust injection along flight corridors into appropriate grid boxes of global 2-D and 3-D models (scale of 1000 km) for the purpose of assessment. The interaction between these different regimes, and how subgrid processes on small scales affect the assessment of large-scale models, are important components of the HSCT assessment effort.

Studies of small-scale processes were carried out for the CIAP assessments during the mid-70's (Hoshizaki et al., 1975; Taylor et al., 1975). These studies included simulations of the chemical evolution of effluents in the far-wake regime (ie., after breakdown of the vortex pair; Gelinas and Walton, 1974), utilizing chemical mechanisms available at the time. The impact of repeated flights along a corridor were also simulated (Taylor et al., 1975) in two ways:
a) the inhomogeneity of gases within a flight corridor was studied by superposing passive tracers calculated for individual plumes from different aircraft with a model including only plume mixing;
b) the chemistry in the corridor was simulated by considering the corridor as a box (400 km x 3 km) with uniform species concentrations mixing with the background atmosphere, and introducing the effluents as a source over the whole box, thus ignoring the inhomogeneities due to single plumes. This study did not include the effect of large-scale advection, nor did it assess the impact of non-linear subgrid processes on global models. Results from this study indicated that, although concentrations of NO_x within the corridor could be enhanced by factors of five over the background, ozone levels within the corridor decreased only by approximately 10%.

Recent modeling efforts funded by the HSRP have concentrated up to now in either the modeling of individual plumes, or global assessment. In particular, large-scale global models have approached the assessment problem by injecting a source of aircraft exhaust gases (primarily $NO_x = NO + NO_2$) into the appropriate grid boxes along the flight path, as prescribed by a given scenario. In this approach, the exhaust gas is assumed to be spread evenly over the whole grid box at steady state, and the photochemical partitioning of nitrogen species and HNO_3 is that prescribed by the chemistry of the background atmosphere. As a result, the impact on ozone calculated by 2-D models is insensitive to the speciation of the adopted aircraft source (NO_x or HNO_3), and depends instead on the background atmospheric dynamics and chemistry, particularly assumptions about heterogeneous chemistry (Prather et al., 1992; Weisenstein et al., 1991). Three-dimensional analysis have considered zonal asymmetries induced by both dynamics and the specific location of the source (Prather, 1992; Douglass et al., 1992) on the distribution of passive tracers from aircraft. The scale in these models is too large to resolve inhomogeneities of specific plumes dispersing into the background atmosphere. However, these studies indicate that enhancements in passive effluents of factors of 2-5 over the calculated zonal mean could occur in regions near flight corridors.

Several factors indicate the need for a reassessment of corridor effects in the context of the HSCT assessment. These include:

1. Our understanding of stratospheric chemistry has changed substantially since the mid-70's. Important developments include the coupling between Cl_x, NO_x, and HO_x species; the role of reservoir species such as $ClNO_3$ and N_2O_5; and the potential importance of heterogeneous mechanisms occurring on ice, nitric acid tri-hydrates, and sulfate aerosols.
2. The chemical partitioning of species within the plume, and the rate of ozone removal is very different from those in the average background atmosphere. Large-scale assessment models must understand the uncertainties in their results introduced by neglect of subgrid processes due to inhomogeneities and non-linearities in the plume chemistry.
3. Enhancement of nitric acid and water along flight corridors could increase the probability of forming nitric acid tri-hydrate particles (Peter et al., 1991). If they form outside the polar vortices, heterogeneous chemistry acting on these PSC-like clouds could process large amounts of mid-latitude air, and thus decrease mid-latitude ozone indirectly through their effect on chlorine chemistry.

The calculations presented in this section address issue (3) above. In particular, we focus on the potential impact of subgrid inhomogeneities within a large-scale model box, and address whether these inhomogeneties would additionally enhance the probability of PSC formation over that calculated by large-scale models.

APPROACH

a) Corridor dimensions

We refer to Fig. 1 to clarify the different scales relevant to the problem considered. This figure illustrates an idealized cross-sectional view perpendicular to flight paths, where advection effects are neglected. Individual plumes from single flights expand as they mix with the background atmosphere; their cross-sectional areas are time dependent, calculated from the Gaussian plume equations in our model (see below). A flight corridor will contain all the individual flight plumes. For most global scale models, we expect that flight corridors will be smaller than the model grid box.

We envision a corridor as a "tube", centered on a given flight path, with horizontal and vertical dimensions l_h^c, l_v^c, with corresponding cross-sectional area A_c. Intuitively, we would choose the dimensions of the corridor to encompass the area perturbed by a given aircraft fleet. These dimensions would then be determined by: a) the spread of individual flight paths around the center of the corridor; b) the spread of individual plumes before they are mixed into the background atmosphere. Since the dimension of individual plumes at the beginning of the wake regime is of order 100 m, and the enhancement of exhaust products such as NO_x,HNO_3, and water is 10 - 100 typical background values, we expect that parameter b) will be of order 10's of km in the horizontal. This is comparable to the expected spread of flight paths, and therefore we expect the horizontal dimension of our corridor (l_h^c) to be of order 10's of km. On the basis of both expected flight path spread, and vertical plume spread, the vertical dimension l_v^c is expected to be a few kilometers.

b) Gaussian plume approximation

We assume that, for the chemically-inactive species water and the family $NO_y = (NO + NO_2 + HNO_3 + 2xN_2O_5 + ClNO_3 + NO_3)$, the spatial dependence of the concentration will be given by a Gaussian of the form:

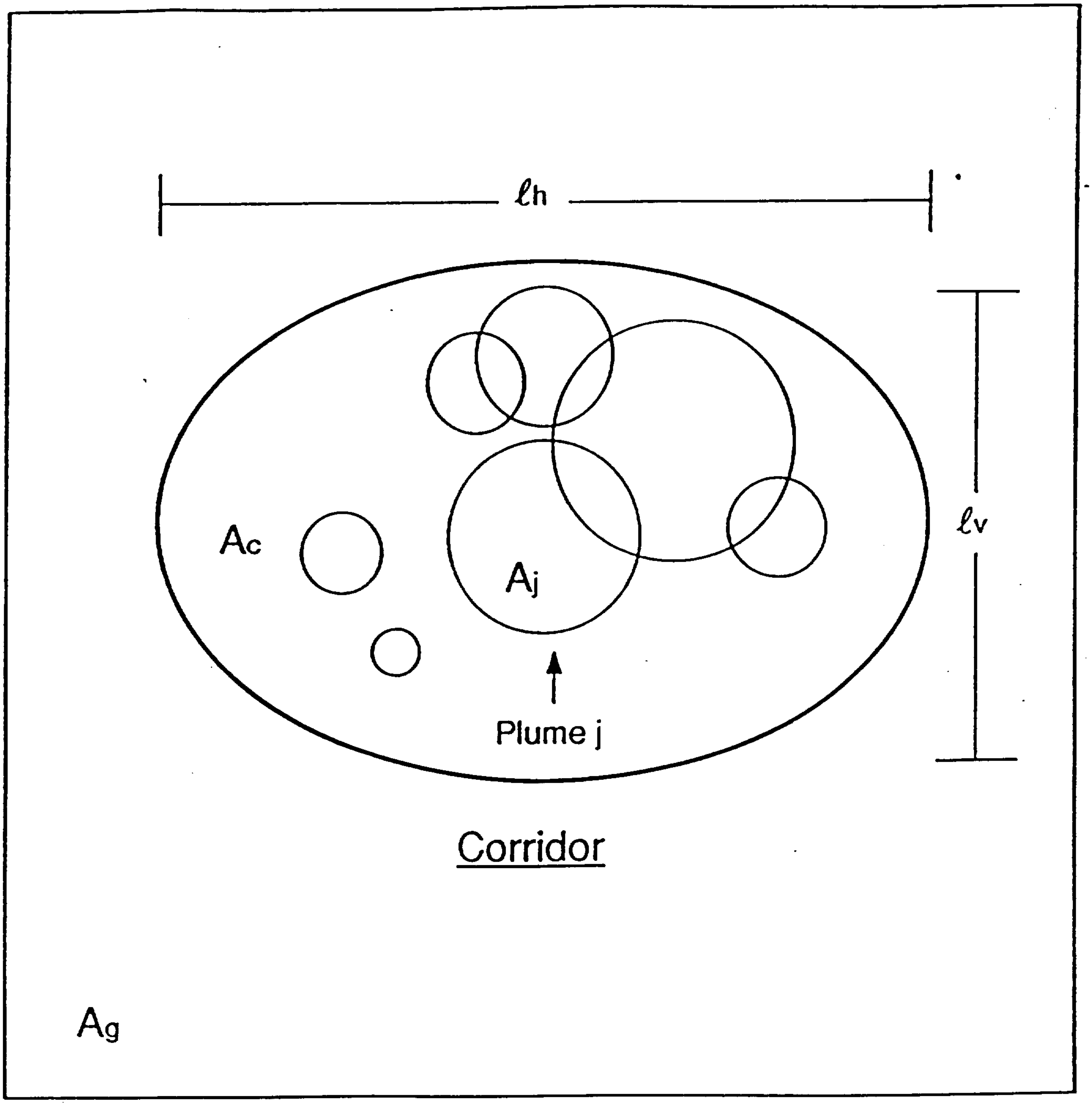

MODEL GRID BOX

Fig. 1: Schematic representation of the different scales of interest to our problem. The corridor with cross-sectional area A_c is defined by the superposition of different individuals plumes j of different age, with A_j. This corridor will in turn be contained in the grid box of a large-scale global model. Direction of flight is perpendicular to the figure plane.

$$c(y,z,t) = c_0(t)e^{-\left(\frac{y^2}{\sigma_y^2} + \frac{z^2}{\sigma_x^2}\right)} \tag{1}$$

where y, and z are horizontal and vertical dimensions relative to the center of the plume. The concentrations c(y,z,t) refer to the *plume* constituents, and should be added to the background concentrations to get the total. The variability along the plume axis is contained in the time dependence. We also note that, as the plume spreads, the vertical and horizontal dimensions $\sigma_{y,z}$ will increase.

The time dependence at plume center and the time development of $\sigma_{y,z}$ are calculated from the formulation described in Chapter 2, in particular equations (1) - (4 in that section. We stress that for the species considered in this particular study (H_2O and NO_y), the P and L terms in equation (1) in Chapter 2 are set equal to zero

b) Corridor effects

At each point along the corridor, concentrations of a given species can be obtained by superposition of plumes from individual flights:

$$C^c(r, t) = \sum_{j=1}^{\infty} \left[c^j\left(r-r_0^j, t + \Delta tj\right)\right] \tag{2}$$

where $c^j(r,t)$ denotes the concentration due to a flight that intersects the plane perpendicular to the flight path at r_σ^j at time t - Δt_j; these concentrations are obtained from the solution of the continuity equation (including chemistry). We also assume for simplicity that the background concentration $c_a(r)$ is constant with time for the domain of interest.

We stress the following points regarding equation (2). Firstly, the terms in the summation representing the older plumes approach zero as $\Delta t_j \to \infty$. The sum can then be approximated by a sum over a finite number of plumes.

We also note that the background concentration $c_a(r)$ must include the large-scale perturbations of the adopted flight scenario. Although in theory such perturbations would be determined by sufficient superposition of individual aircraft plumes, calculation of such an effect is cumbersome because: 1) given the lifetime of the species under consideration, aircraft plumes would have to be superimposed over periods of over a year; 2) mixing parameters at scales of 100-1000 km would have to be considered. Modeling of concentrations at these scales are best achieved by multi-dimensional models. We thus *assume* that the concentrations at these scales have been calculated by such models, and calculate the additional small-scale, subgrid perturbations to this background due to the superposition of plumes before the mix into the background. We note that, for chemically-inert species considered in this case study, and assuming the preservation of a Gaussian distribution, the time development of the perturbation over background concentrations is independent of the chosen background.

DESCRIPTION OF CALCULATIONS

The effects of plume superposition on water and NOY are calculated from equation (2) using the single-plume calculations described in Chapter 2. The results presented below assume $K_{ym} = K_{zm} = 10^3$ cm^2 s^{-1} in Equation (4) of Chapter 2. Initial spreads for the plume of $\sigma_{y,z}$ = 70 m are adopted. All other parameters are chosen as described in that Appendix. We also adopt the upper limit for dilution of water and NO_y, as described in that section.

We have carried out two sets of calculations. The first set considers a maximum superposition scenario where subsequent flight paths exactly coincide. This case would give the maximum absolute perturbation, but it would be distributed over a small spatial region.

A more realistic scenario is one in which flight paths occur randomly over a given region. We thus assume that the location of a given flight path is uniformly and randomly distributed over a region 20 km in the horizontal and 2 km in the vertical, perpendicular to the flight paths. Sensitivity calculations indicate that the small-scale structure calculated with this assumption would essentially be the same if we chose a larger box size.

RESULTS

The calculated perturbations concentrations c for H_2O and NO_y are shown in Figs. 2a and 2b, respectively, assuming exact superposition of aircraft flight paths and a frequency of two flights per day. Other calculations (not shown) indicate that the results scale linearly with flight frequency.

The results in Fig. 2 are shown as a function of total number of flight days superimposed. Because of the relatively decay time the plume (about 3 days, see Fig. 2, Chapter 2), the calculated concentration increases rapidly during the first 5 days, and slows down subsequently due to the superposition of small residuals from old plumes.

These calculations indicate enhancements of about two orders of magnitude for both water and NO_y over background values. We note, however, that the scale of this enhancement is of the order $\sigma_{y,z}$= 100's of meters. Such perturbations would thus be insignificant for any kind of large-scale impact.

Figures 3a - 3e show the calculated perturbations to background water (ppmv) for flights occurring randomly over a corridor 20 km wide and 2 km high. This corridor is embedded into a larger box 30 km wide and 5 km high to keep track of the "leakage" of plume material out of this box. Both boxes are gridded into square cells 50 m on the side. A random number generator is used to distribute flights over the cells in the inner box. A frequency of two flights per day is adopted.

The panels show the superposition of plumes after 5 days (panel a), 10 days (b), 30 days (c), 85 days (d) and 90 days (e) of flights. Contours are given at 0.2, 0.5, and 1 ppmv (dashed contour) perturbation. The results presented below assume $K_{ym} = K_{zm} = 10^3$ cm^2 s^{-1} in Equation (4) of Chapter 2. All other parameters are chosen as described in that Appendix. We also note that the NO_y perturbations have the same distribution, with a scaling factor of 1.6×10^{-3}. The calculated perturbations should be compared to background values of about 4 ppmv for water and 10 ppbv for NO_y. The additional NO_y could be mostly in the form of HNO_3 if vigorous heterogeneous chemistry would occur on contrails during the early stages of the wake.

Comparison of the panels in Fig. 3 indicates that, after about 30 days of flights, a small-scale pattern emerges. About 10 cells with water perturbations > 0. 5 ppmv (NO_y > 0.8 ppbv) are randomly distributed over the corridor. The spatial extent of these cells is of order 0.5 km. Comparison of the day 85 versus day 90 results indicates that the 0.5 ppmv H_2O (0.8 ppbv NO_y) contours have a lifetime of at least 5 days. On the other hand, the 1 ppmv H_2O (1.6 ppbv NO_y) perturbations last for less than 5 days. After 90 days of flights, we also note a larger-scale perturbation of 0.2 ppmv (0.32 ppbv NO_y) extending over the whole flight corridor and expanding into the larger box. We note, however, that at these time and spatial scales we must start considering the impact of large-scale diffusion and advection over the corridor. The calculations presented are thus relevant only for the smaller scales.

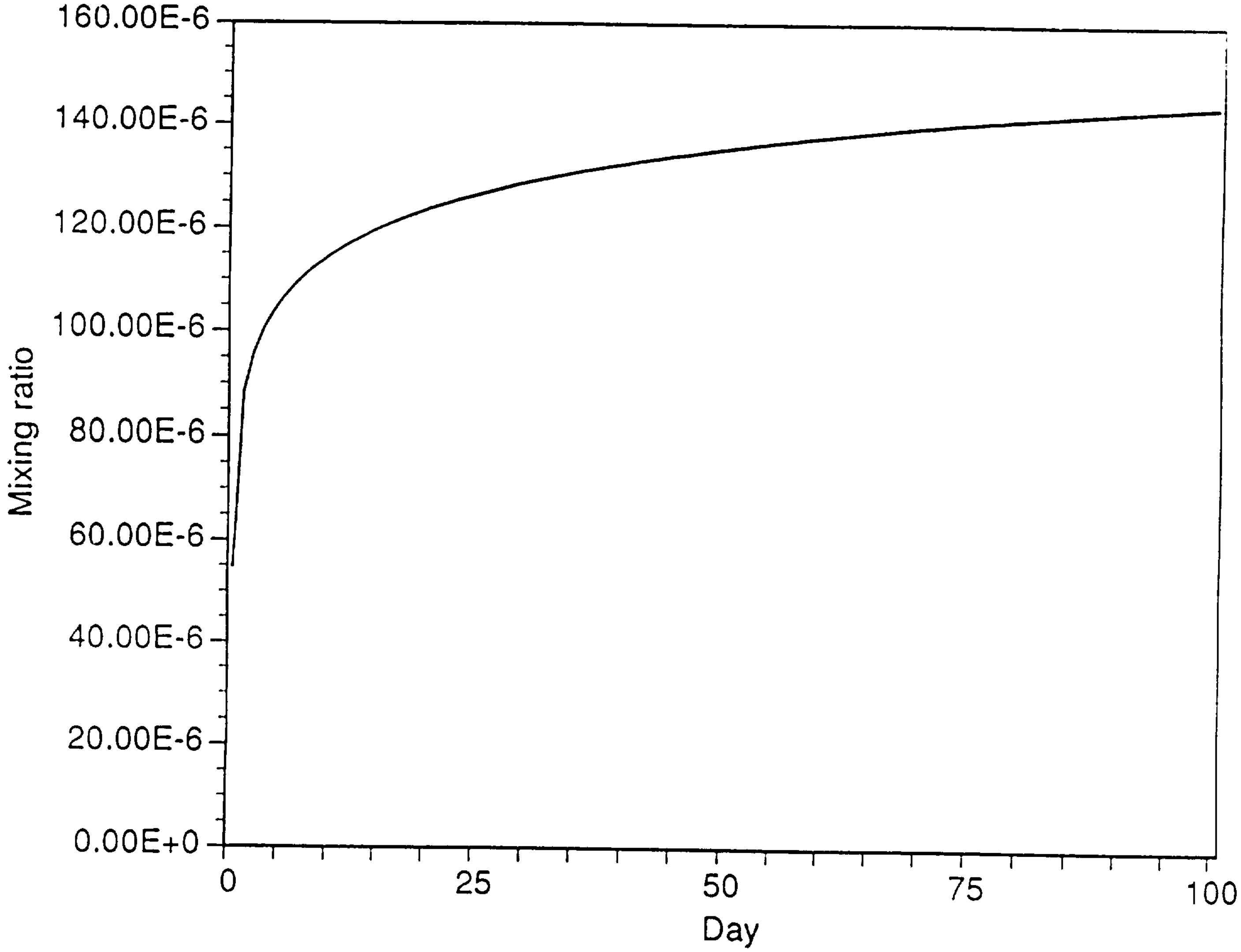

Fig. 2a: Calculated perturbations to concentrations of water (a) and NO_y (b) for a flight frequency of 2 flights per day. We assume that flight paths coincide exactly in space. The concentrations are plotted as a function of total number of flight days superimposed.

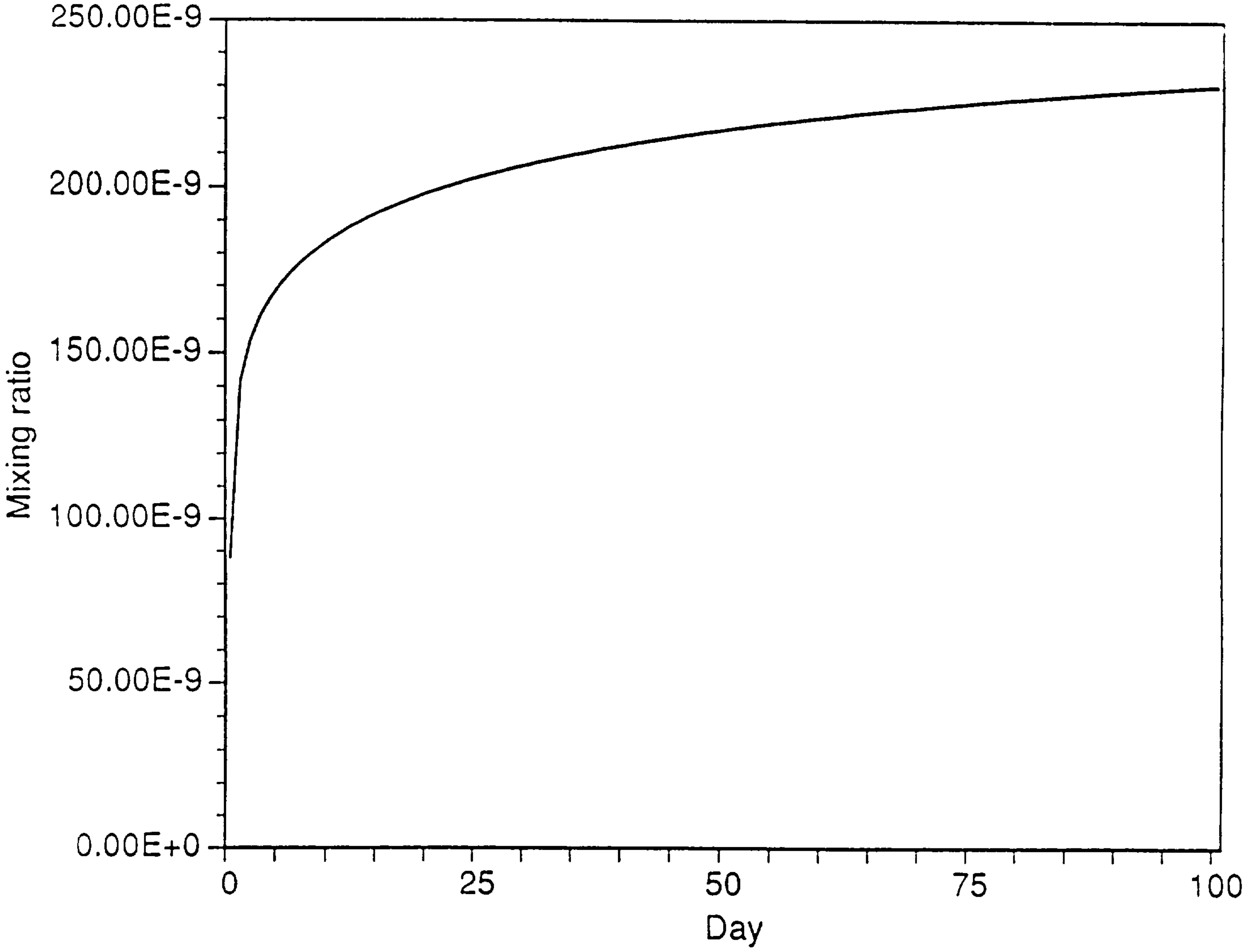

Fig. 2b: Calculated perturbations to concentrations of water (a) and NO_y (b) for a flight frequency of 2 flights per day. We assume that flight paths coincide exactly in space. The concentrations are plotted as a function of total number of flight days superimposed.

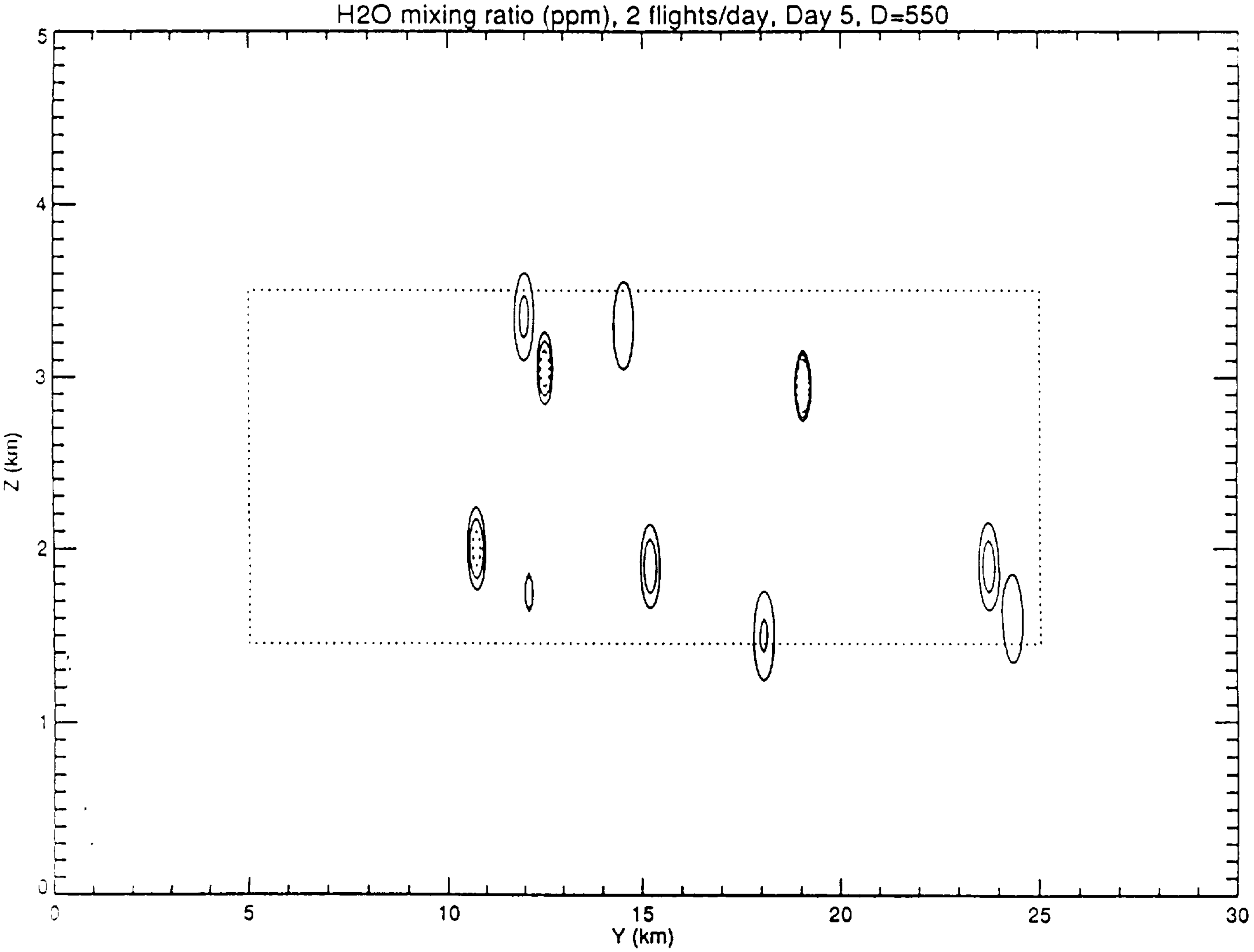

Fig. 3a: Calculated perturbations to concentrations of water, for flights distributed randomly over an area 20 km in the horizontal and 2 km in the vertical (dotted box). Contours are for perturbations of 0.2 ppmv, 0.5 ppmv, and 1 ppmv (dotted contour) above background. Similar structures are obtained for NO_y by multiplying contour values by 1.6×10^{-3}. Panels correspond to superposition of flights for a total of 5 days (a), 10 days (b), 30 days (c), 85 days (d), and 90 days (e). See text for further details.

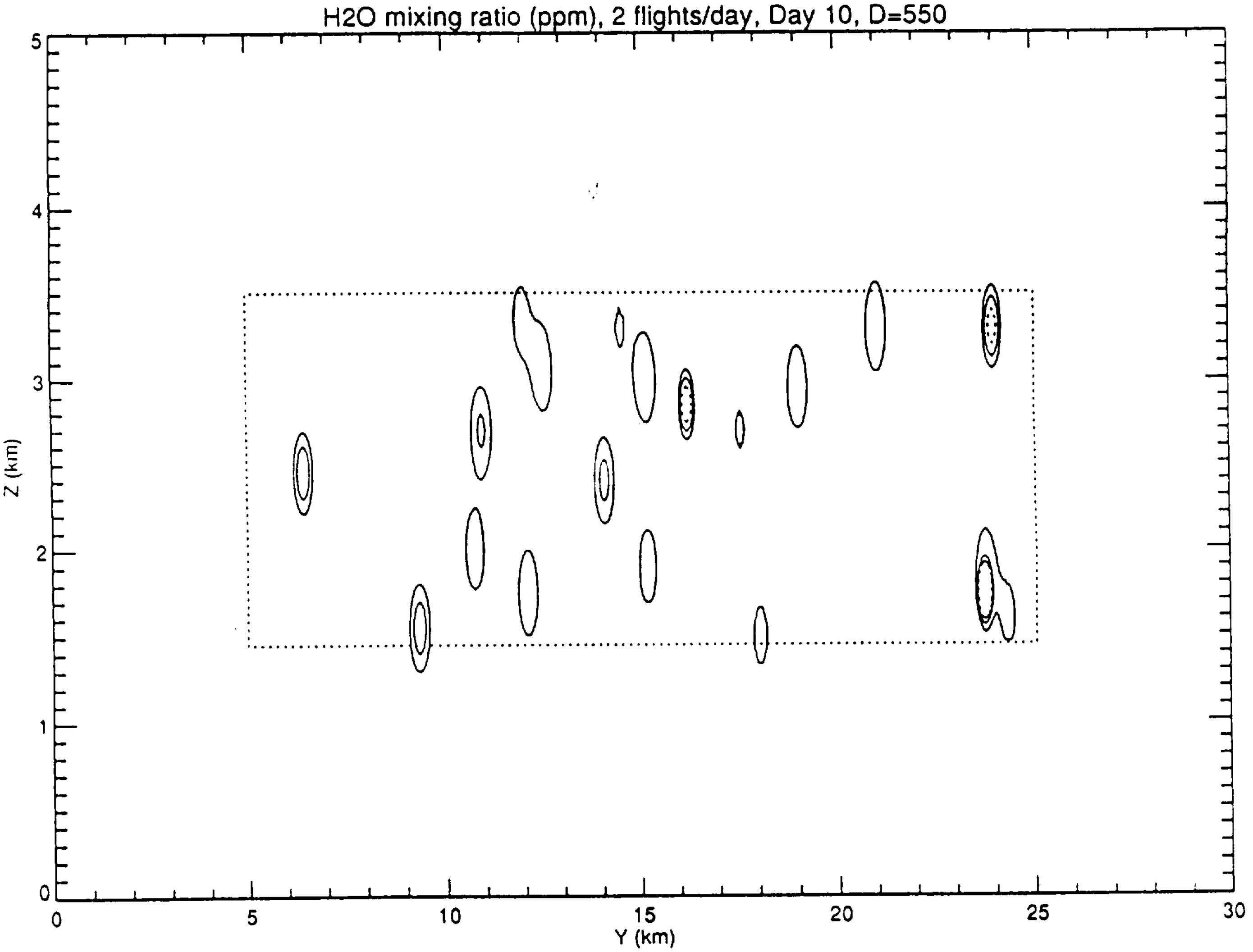

Fig. 3b: Calculated perturbations to concentrations of water, for flights distributed randomly over an area 20 km in the horizontal and 2 km in the vertical (dotted box). Contours are for perturbations of 0.2 ppmv, 0.5 ppmv, and 1 ppmv (dotted contour) above background. Similar structures are obtained for NO_y by multiplying contour values by 1.6 x 10^{-3}. Panels correspond to superposition of flights for a total of 5 days (a), 10 days (b), 30 days (c), 85 days (d), and 90 days (e). See text for further details.

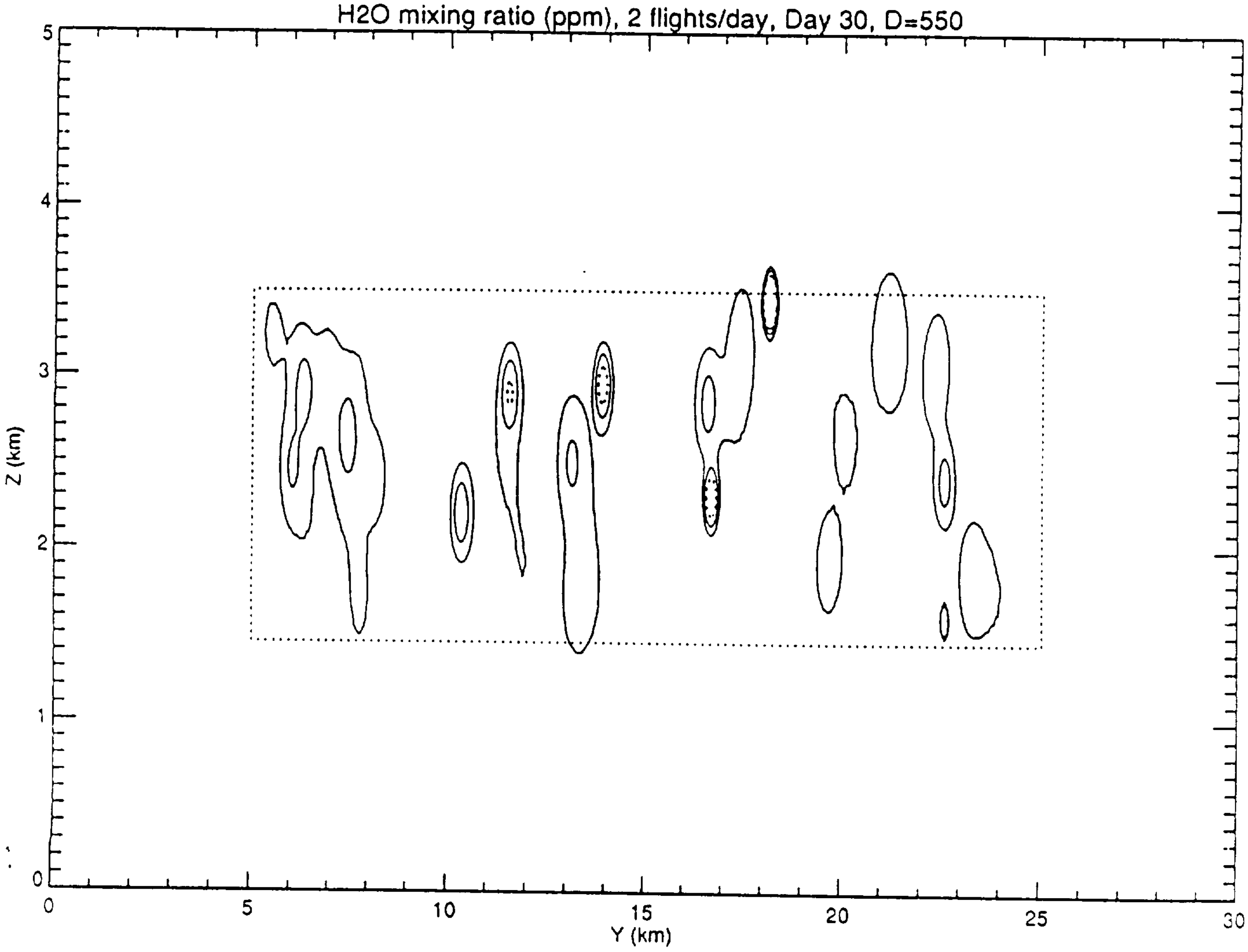

Fig. 3c: Calculated perturbations to concentrations of water, for flights distributed randomly over an area 20 km in the horizontal and 2 km in the vertical (dotted box). Contours are for perturbations of 0.2 ppmv, 0.5 ppmv, and 1 ppmv (dotted contour) above background. Similar structures are obtained for NO_y by multiplying contour values by 1.6×10^{-3}. Panels correspond to superposition of flights for a total of 5 days (a), 10 days (b), 30 days (c), 85 days (d), and 90 days (e). See text for further details.

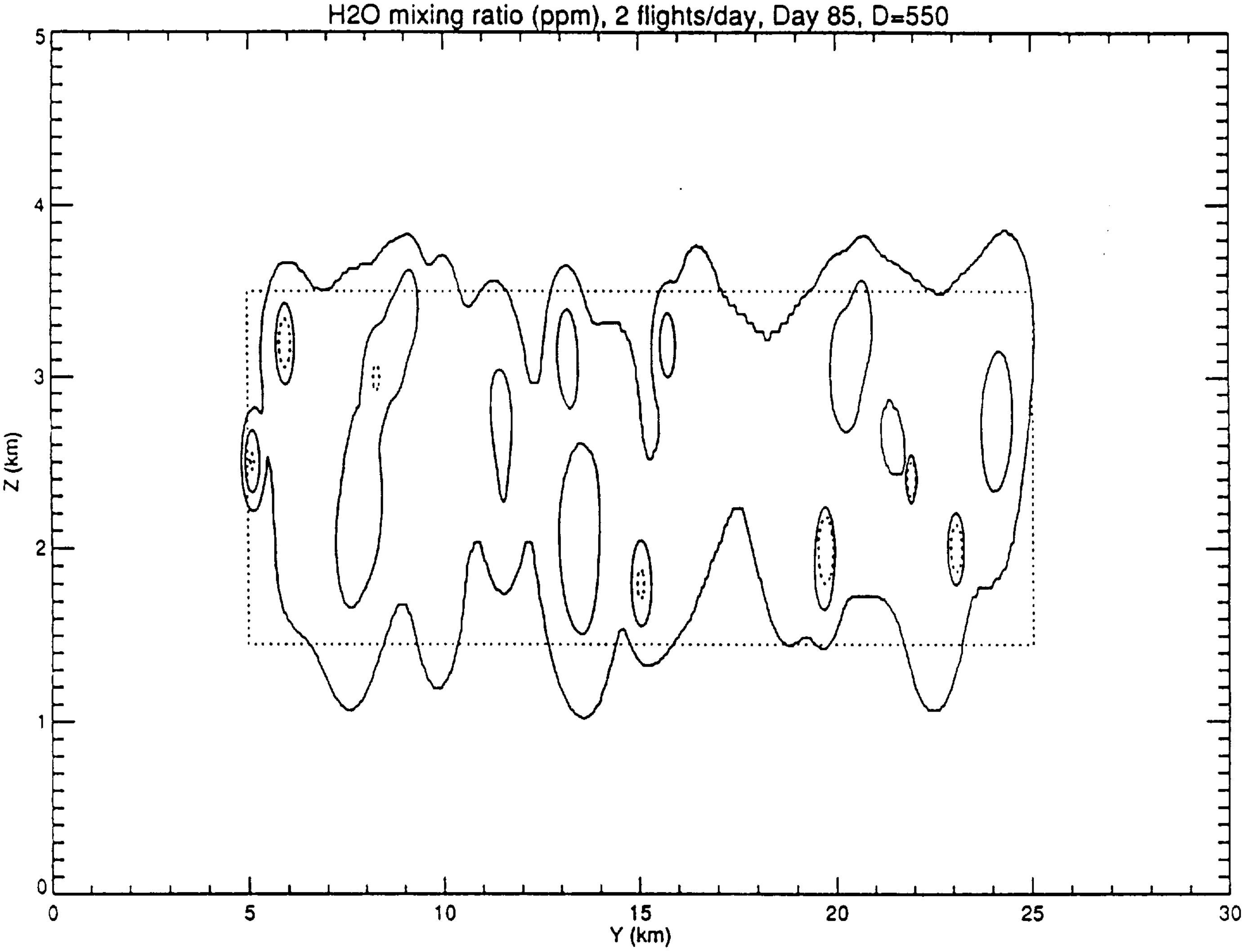

Fig. 3d: Calculated perturbations to concentrations of water, for flights distributed randomly over an area 20 km in the horizontal and 2 km in the vertical (dotted box). Contours are for perturbations of 0.2 ppmv, 0.5 ppmv, and 1 ppmv (dotted contour) above background. Similar structures are obtained for NO_y by multiplying contour values by 1.6×10^{-3}. Panels correspond to superposition of flights for a total of 5 days (a), 10 days (b), 30 days (c), 85 days (d), and 90 days (e). See text for further details.

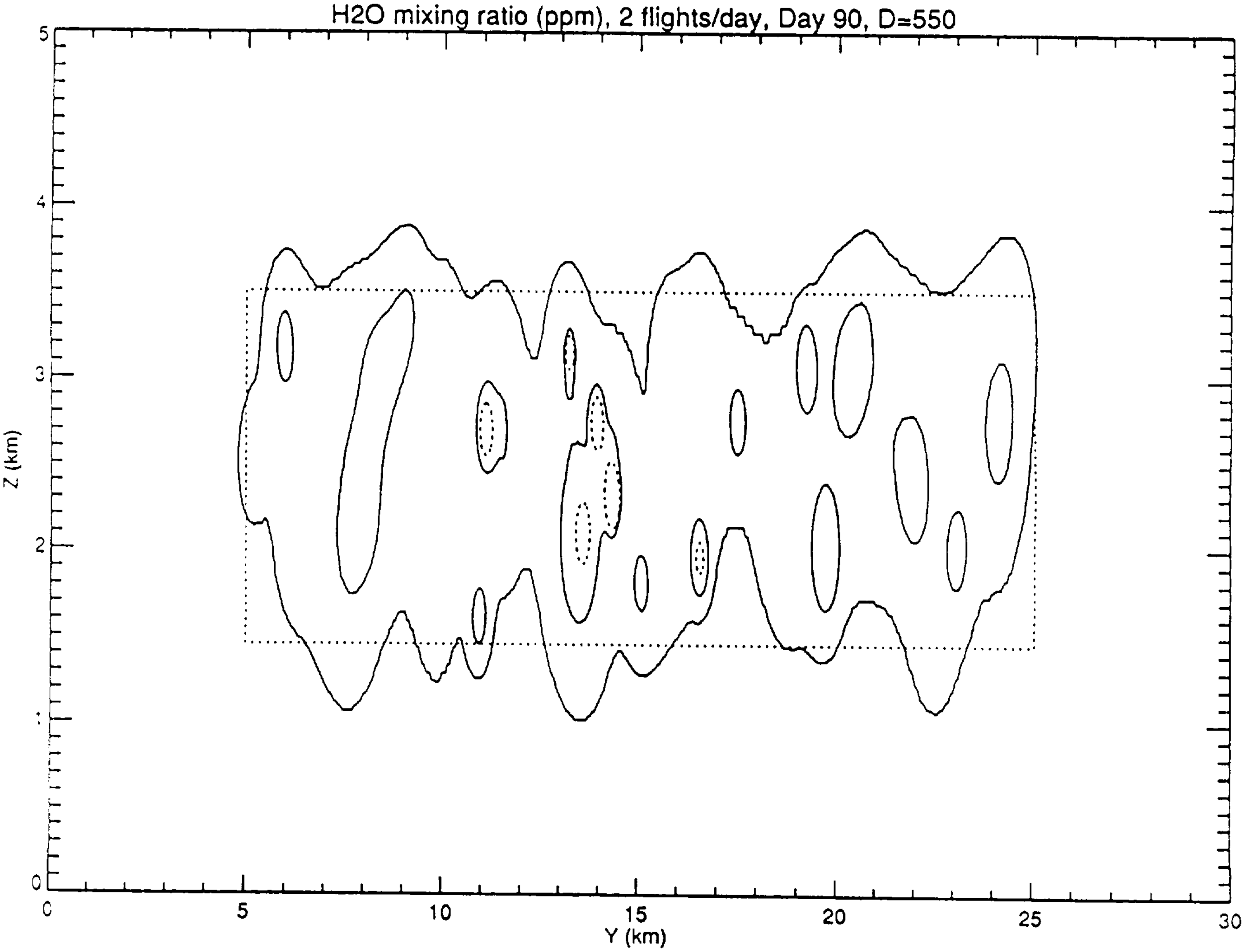

Fig. 3e: Calculated perturbations to concentrations of water, for flights distributed randomly over an area 20 km in the horizontal and 2 km in the vertical (dotted box). Contours are for perturbations of 0.2 ppmv, 0.5 ppmv, and 1 ppmv (dotted contour) above background. Similar structures are obtained for NO_y by multiplying contour values by 1.6×10^{-3}. Panels correspond to superposition of flights for a total of 5 days (a), 10 days (b), 30 days (c), 85 days (d), and 90 days (e). See text for further details.

DISCUSSION AND CONCLUSIONS

Two-dimensional model results indicate increases in the latitudinal average concentrations of order 25% and 70% for water and NO_y, respectively, at Northern latitudes near the flight corridors. Such increases would lead to an increase in the saturation temperature for nitric acid trihydrate of about 2-3 K, using the equilibrium equation of Hanson and Mauersberger (1988). Three-dimensional models indicate that passive tracers could exhibit local enhancements 2-3 times larger than zonal averages. Such enhancements could lead to increases in the trihydrate saturation temperature of order 5K. Analysis by Peter et al. (1991) of temperature statistics within the Northern Polar vortex, coupled with more detailed modeling of PSC nucleation suggested that such enhancements in water and NO_y could lead to an increase in the probability of occurrence of PSCs by factors of 2-4.

We estimate that an additional enhancement of 0.5-1 ppmv H_2O and 0.8-1.6 ppbv HNO_3 would lead to an additional increase of about 0.5 - 1K in the saturation temperature for nitric acid trihydrate. According to the results in Fig. 3, such perturbations will extend over length scales of order 500 m, and last for 1-5 days. Estimates for nucleation times for PSCs at small supersaturation are of order of hours (Peter et al., 1991). Furthermore, conversion of HCl to active chlorine by heterogeneous reactions on PSCs occurs with time constants of hours to days (Turco et al., 1989).

The above analysis suggests additional that subgrid-scale PSCs could be produced within flight corridors. Quantitative assessment of this effect would require the input in these calculations (ie., spatial and temporal scale of subrid features). Additionally, we need estimates of temporal and spatial scales of temperature fluctuations and processing rates by entrainment of air into these structures. It is thus difficult to quantify the importance of these processes, although they cannot be ruled out from the analysis carried out in the above report.

REFERENCES

1. Douglass, A.R., R.B. Rood, C.J. Weaver, (1992) Global mass transport characteristics determined from model tracer experiments. Presented at the Eighth Conference on the Middle Atmosphere, American Meteorological Society, Atlanta, GA, January 5-10, 1992.

2. Gelinas, R.J. and J.J. Walton (1974) Dynamic-kinetic evolution of a single plume of interacting species. *J. Atmos. Sci.*, **31**, 1807.

3. Hanson, D.R. and K. Mauersberger (1988) Laboratory studies of the nitric acid trihydrate: Implications for the South polar stratosphere. *Geophys. Res. Lett.*, **15**, 855-858.

4. Hoshizaki, H., L.B. Anderson, R.J. Conti, N. Farlow, J.W. Meyer, T. Overcamp, K.O. Redler, and V. Watson (1975) Aircraft wake microscale phenomena. Chapter 2 in CIAP Monograph 3, Department of Transporation, Washington, DC, DOT-TST-75-53.

5. Peter, Th., C. Brühl and P.J. Crutzen (1991) Increase in the PSC-Formation probability caused by high-flying aircraft. *Geophys. Res. Lett.*, **18**, 1465-1468.

6. Prather, M.J. (1992) The atmospheric effects of stratospheric aircraft: assessing the impact of a projected fleet of high-speed civil transports. Presented at the Eighth Conference on the Middle Atmosphere, American Meteorological Society, Atlanta, GA, January 5-10, 1992.

7. Taylor, T.D., J.S. Chang, T.V. Crawford, G.R. Hilst, H. Hoshizaki, J. Riley, J.J. Walton, and G. Widhopf (1975) Dispersion and transport at intermediate scales between the microscale and the horizontal mesoscale. Chapter 3 in CIAP Monograph 3, Department of Transporation, Washington, DC, DOT-TST-75-53.

8. Turco, R.P., O.B. Toon, P. Hamill (1989) Heterogeneous physicochemistry of the polar ozoen hole. *J. Geophys. Res.*, **94**, 16,493-16,510.

9. Weisenstein, D.K., M.K.W. Ko, J.M. Rodriguez, and N.D. Sze (1991) Impact of heterogeneous chemistry on model-calculated ozone change due to high speed civil transport aircraft. *Geophys. Res. Lett.*, **18**, 1991-1994.

CHAPTER 4
LABORATORY STUDIES OF STRATOSPHERIC HETEROGENEOUS CHEMISTRY

INTRODUCTION

The purpose of this aspect of our program is to evaluate the role of heterogeneous chemistry relating to the potential atmospheric effects of emissions from a fleet of supersonic aircraft flying in the stratosphere. Research needs in this area are motivated by a relative lack of knowledge of chemistry on or in aerosol particles compared to that of the homogeneous gas phase. Significant advances in our understanding of heterogeneous chemical mechanisms are required for quantitative prediction of stratospheric chemistry with or without added aircraft emissions.

Heterogeneous chemistry has been a key issue in stratospheric photochemistry since the discovery of the role that polar stratospheric clouds (PSCs) play in the so-called 'ozone hole' over Antarctica. It is now understood that heterogeneous chemistry perturbs the balancing of the NO_x/Cl_x cycles, tending to deactivate NO_x (by producing HNO_3) while activating Cl_x (by converting $ClONO_2$ and HCl to HOCl and Cl_2). During the Antarctic winter, extremely cold temperatures (T < 190K) push this chemistry to an extreme by forming ice particles large enough to sediment out to the stratosphere, thus removing NO_y while leaving behind high ClO levels which destroy ozone in September/October after the return of sunlight in the spring.

Globally, the question is what is the impact of analogous chemistry on background aerosol particles, which compose the Junge layer of sulfuric acid / water particles at 18 to 25 km throughout the stratosphere. In particular, it now appears that the reaction of N_2O_5 with H_2O in condensed H_2SO4/H_2O particles,

$$N_2O_5(g) + H_2O(s) \text{ ---> } 2HNO_3 \qquad \text{R1}$$

effectively shifts the photochemical partitioning of gas phase NOy species (NO, NO_2, NO_3, N_2O_5, HNO_3) toward HNO_3. In contrast, heterogeneous reactions of $ClONO_2$ and HCl,

$$ClONO_2(g) + H_2O(s) \text{ ---> } HOCl(s) + HNO_3 \qquad \text{R2}$$

$$HCl(g) \text{ ---> } HCl(s) \qquad \text{R3}$$

$$HOCl(s) + HCl(s) \text{ ---> } Cl_2 + H_2O \qquad \text{R4}$$

are relatively slow and ineffective on background aerosols.

Recent modeling indicates that reaction R1 shifts the balance of the NO_x / Cl_x chemical enough to account for the downward trend in global ozone observed over the last decade (Rodriguez et al., 1991). However, without significant activation of Cl_x via R2-R4, dramatic ozone depletion such as is observed over Antarctica is not possible. It is clear that the heterogeneous kinetics underlying R1-R4 need to be characterized as accurately as possible.

This chemistry has major implications for HSCT assessment. Two dimensional modeling of reaction R1 indicates that emission of NO_x into the stratosphere at 17-20 km from an HSCT fleet would have minimal impact on ozone levels (Weisenstein et al., 1991). The key issue there actually involves degree of transport of emissions above the aerosol layer. More generally, HSCT assessment requires understanding of potential perturbation of the aerosols themselves due to both NO_x (i.e. HNO_3) and H_2O emissions, particularly in flight corridors.

The latter issue is best put in perspective by comparing winter time chemistry over the Arctic and Antarctic. Temperatures over the Arctic are cold enough ($T \geq 190K$) to form so-called Type I PSCs which are believed to be composed of hydrates of nitric acid. While these PSCs do activate Cl_x via R2-R4 during the dark of winter, the PSCs (and activated ClO) dissipate in the spring before the solar flux can deplete ozone. The crucial difference between the Arctic and Antarctic winter is the colder temperature in the latter, which form ice particles (Type II PSCs) which can remove HNO_3 by sedimentation. A key issue for HSCT assessment is whether HSCT emissions can perturb PSC climatology and lead to (mid-latitude) PSC nucleation in the presence of sunlight.

Thus, this project has investigated two separate issues relating to HSCT assessment: (1) What are the detailed kinetics of reactions R1-R4 on sulfuric acid / water surfaces representative of background stratospheric aerosols? (2) What are the composition and nucleation properties of the hydrates of hydrates of nitric acid that are presumed to compose Type I PSCs? The following sections detail the laboratory projects that investigated these issues.

GAS UPTAKE BY SULFURIC ACID DROPLETS

There have been a number of studies of reactions R1-R4 on sulfuric acid surfaces in various laboratories. For N_2O_5 reaction with $H_2O(s)$ (R1) reactivity coefficients, γ (defined as the probability of reaction upon collision with the liquid surface), on the order of 0.06 to 0.14 have been reported (Mozurkewich and Calvert, 1988; Van Doren et al, 1991; Hanson and Ravishankara, 1991), with little apparent dependence on sulfuric acid composition or temperature. Reaction of $ClONO_2$ with $H_2O(s)$ (R2) on the other hand has a strong dependence on sulfuric acid composition (Tolbert et al., 1988; Hanson and Ravishankara, 1991), while reactions of HCl (R3 and R4) appear to be severely constrained by limited HCl solubility (Watson et al., 1990; Hanson and Ravishankara, 1991).

What was lacking in all these studies was a systematic study of the dependence of these reactions on both sulfuric acid temperature and composition. Previous studies had effectively sampled relevant stratospheric conditions that roughly span 60 to 80 wt% H_2SO_4 from 230 to 210 K. It is important to note that temperature and composition are not independent, since they are coupled by equilibration with ambient water vapor.

Previously we investigated the uptake of N_2O_5 (Van Doren et al, 1991) and HCl (Watson et al., 1990) on liquid sulfuric acid at room temperature. This work was part of an on-going collaboration between Aerodyne Research, Inc., and Boston College to study heterogeneous kinetics utilizing a technique based on producing fast-moving liquid droplets. For this project, the goal was to construct a modified apparatus capable of studying cold sulfuric acid solutions at temperatures approaching the stratosphere. Both temperature and sulfuric acid composition were systematically varied in order to permit extrapolation to a range of stratospheric conditions.

In the next sections we discuss the experimental technique and the modified apparatus designed for this project. Discussion of results for HCl, N_2O_5 and $ClONO_2$ uptake follow.

Droplet Apparatus

A schematic the droplet apparatus is shown in Figure 1. Gas uptake is measured by passing a highly controlled train of droplets through a low pressure flow reactor which contains the trace gas species of interest entrained in a flowing carrier gas of water vapor and helium. This fast moving stream of small monodispersed droplets is produced in a separate chamber by a vibrating orifice jet. Droplets range in diameter from 100 to 250μm. The concentration (n_g) of the trace gas is monitored as the surface area of the droplets passing through the flow tube is changed in a stepwise fashion. The density of the species is monitored downstream of the flow tube via infrared absorption in a multipass 'White' cell coupled to a tunable diode laser system. A

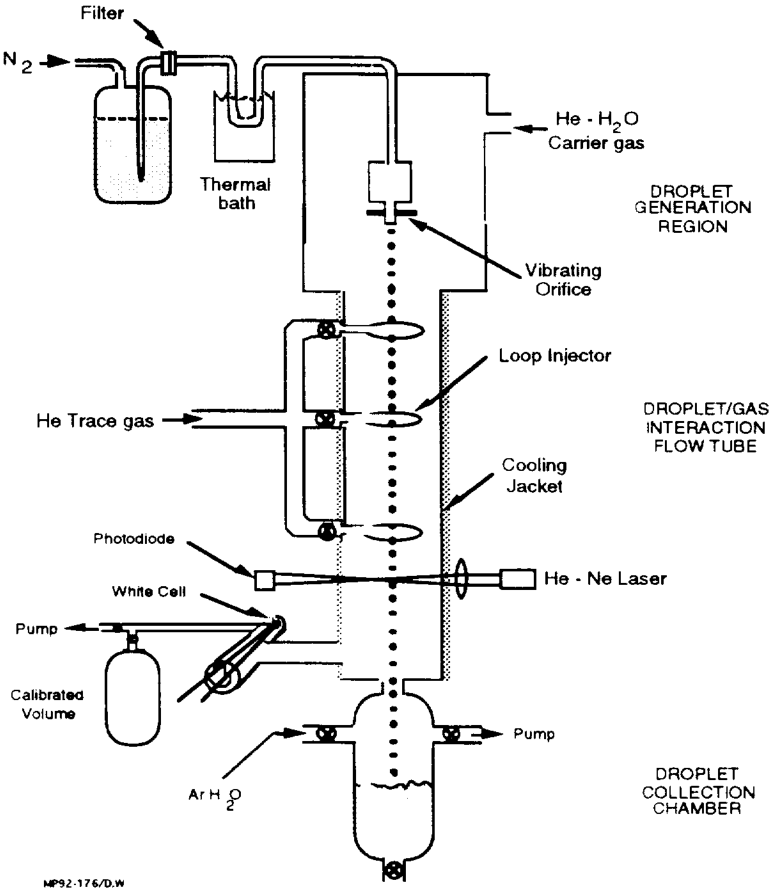

Figure 1. Schematic of droplet apparatus with diode laser detection.

measured decrease in the trace gas signal (Δn_g) resulting from an increase in the exposed droplet surface area corresponds to an uptake of the gas by the droplet surface.

From the basic definition of uptake coefficient in terms of the gas flux (J) into a surface, $\gamma_{meas} = 4J/n_g c$ (see Eq.2-2) we obtain (See Worsnop et al. 1989).

$$\gamma_{meas} = \frac{4 F_g}{c\Delta A} \ln\left(\frac{n_g}{n_g'}\right) \qquad (1)$$

Here F_g is the carrier gas volume rate of flow ($cm^3\ s^{-1}$) through the system, c is the trace gas average thermal velocity (cm s^{-1}), ΔA is the change in the total droplet surface in contact with the trace gas (cm^2), and n_g and n_g' are the trace gas densities (cm^{-3}) at the inlet and outlet of the flow tube respectively (i.e., $n_g = n_g' + \Delta n_g$).

In the droplet apparatus the speed of the droplets is high, in the range of 2000 cm s^{-1}, resulting in a short droplet transit time through the reaction zone. The gas-droplet interaction time, which depends on the gas inlet and the droplet velocity, can be varied from about 2 ms to 20 ms. The short transit times in the droplet apparatus make that device suitable for measuring gas-liquid interactions of species with uptake coefficients: $\gamma > 10^{-3}$.

Specific apparatus modifications/improvements made during this project to permit study of gas uptake into cold sulfuric solution include:

- Liquid delivery system was redesigned to enable flowing cold H_2SO_4 which has high fluid viscosity. This involved both enhanced cooling and improved, high pressure tubing for H_2SO_4 transport.

- A new droplet source nozzle assembly was constructed to minimize corrosion by H_2SO_4 and to extend temperature control to lower temperatures while maintaining spatial stability. The latter is crucial for long term signal averaging of experimental data.

- A new gas flow tube was designed. This tube is aligned longitudinally with the droplets to extend both gas uptake sensitivity and liquid/gas exposure time control. Also, the plumbing of this tube permits in situ cleaning, which is essential for cold sulfuric droplet experiments.

- The new droplet collection and disposal system was put in place to permit both better temperature control and safer, more efficient waste disposal. The latter reflects increasing emphasis on and regulation of laboratory safety.

- Based on the latest developments in diode laser technology at Aerodyne (Worsnop et al., 1992), the infrared absorption system has been upgraded. This involved reconfiguring the laser/White cell/monochromator set-up to ease alignment and to enhance long term stability of the laser. Fast sweeping of diode laser frequency was added to the computer control system in order to 'beat' low frequency noise in the laser system. Non-linear least squares curve fitting was included in data analysis of absorption spectra to improve signal precision (see Worsnop et al., 1992).

A key aspect of the implementation of these modifications involved systematic measurements of water vapor densities as a function of droplet size, composition and temperature. Just as in the stratosphere, the liquid droplet surface equilibrates with ambient water vapor. However, because the fast-moving droplets are exposed to the gas for only ~40 msec, the equilibration is not complete. Thus, understanding of droplet surface temperature and composition requires some modeling of molecular and thermal diffusion within the droplet. In the ideal experiment, appropriate addition of water vapor to the carrier gas flow minimizes perturbation to the initial droplet composition and temperature. This was verified experimentally.

Experiments were performed on sulfuric acid droplets of composition varying from 40 to 70 wt% and of temperatures from 230 to 270K.

HCl Accommodation and Solubility

As discussed above, reactivity of HCl on stratospheric aerosol could have a significant impact on stratospheric photochemistry. Previous studies had indicated that relatively low uptake of HCl into sulfuric acid solution indicated low solubility (Watson et al., 1991; Hanson and Ravishankara, 1991). The purpose of this project was to systematically determine that solubility.

The net uptake of gas (represented by γ_{meas} in eqn. 2) observed in any gas/liquid mass transport experiment is a convolution of many processes. In the simplest case, this net mass transport rate depends on the rates of gas diffusion of the trace gas to the liquid surface, on mass accommodation (e.g. sticking) on the liquid surface, and on the solubility of the gas within the bulk liquid. We express these rates of gas diffusion, accommodation and solubility as the dimensionless coefficients γ_{diff}, α and γ_H, respectively, which are combined in the equation (Worsnop et al., 1989)

$$\frac{1}{\gamma_{meas}} = \frac{1}{\gamma_{diff}} + \frac{1}{\alpha} + \frac{1}{\gamma H} = \frac{\bar{c}d_f}{8D_g} + \frac{1}{\alpha} + \frac{\bar{c}}{4RTH}\left(\frac{t}{D_l}\right)^{1/2} \tag{2}$$

This equation adds the inverses of the coefficients as a series of resistances that sum to give the measured resistance to gas uptake γ_{meas}. The right hand side gives steady state expressions for each of these resistances: (γ_{diff}) the mean molecular speed (c), an effective droplet diameter (d_f, see Worsnop et al., 1989) and the gas diffusion coefficient (Dg); (γ_H) the Henry's law solubility of the gas (H), the liquid diffusion coefficient (D_l) and the gas/droplet exposure time (t). The γ_H term accounts for evaporation of dissolved species which depends both on H and D_l.

From eqn. 3, a plot of $1/\gamma_{meas}$ versus $t^{1/2}$ should give a straight line. Representative data is shown in Figure 2, which shows uptake measurements for HCl into 50 wt% H_2SO_4/H_2O solution at four temperatures (Robinson et al., 1992). The linearity of this $t^{1/2}$ plot confirms that the decrease in observed uptake of HCl with longer liquid/gas exposure time is a diffusion limited process. The change in slope with temperature reflects increasing solubility with decreasing temperature. From equation (3), the slope and intercept of the lines can be used to determine H (Watson et al, 1990) and α (Jayne et al., 1992).

Figure 3 plots the temperature dependence of HCl solubility in H_2SO_4 solutions as derived from the slopes of lines such as those plotted in Figure 2. The solubility has a inverse dependence with both temperature and sulfuric acid composition. The new data is consistent with our previous

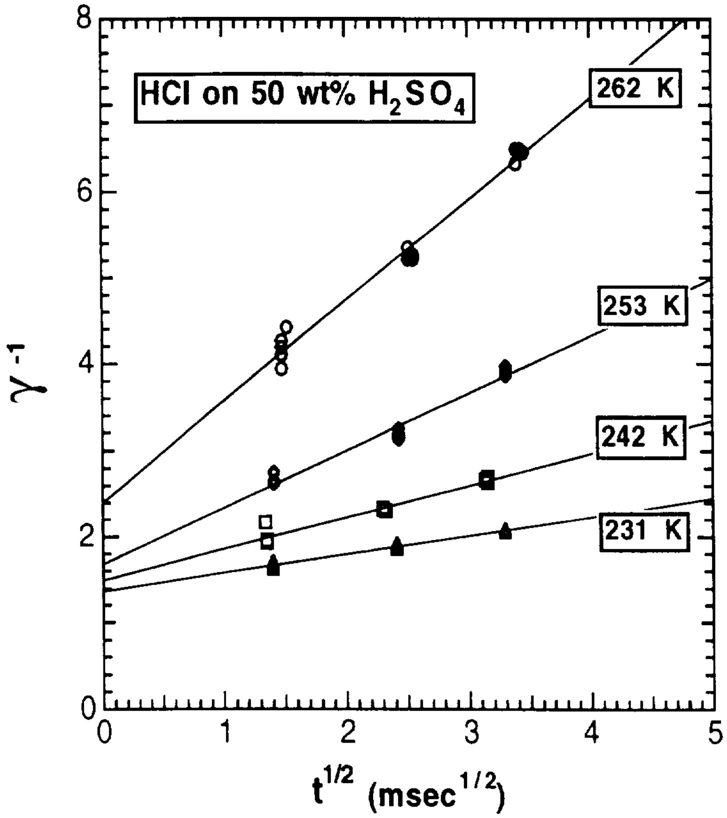

Figure 2. HCl Uptake into 50 wt% H_2SO_4 / H_2O solution (equation 3).

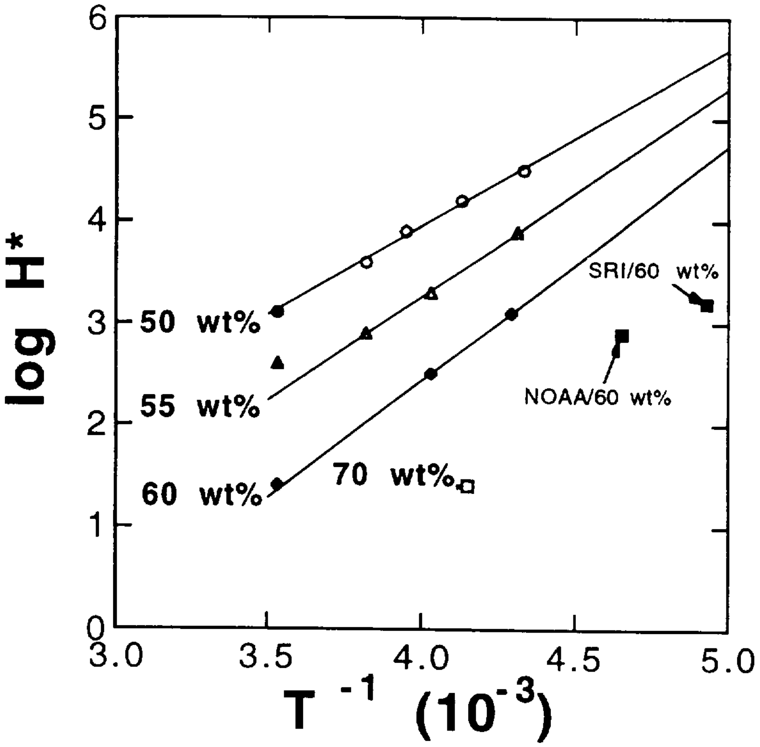

Figure 3. Temperature dependence of HCl Solubility in H_2SO_4 solution.

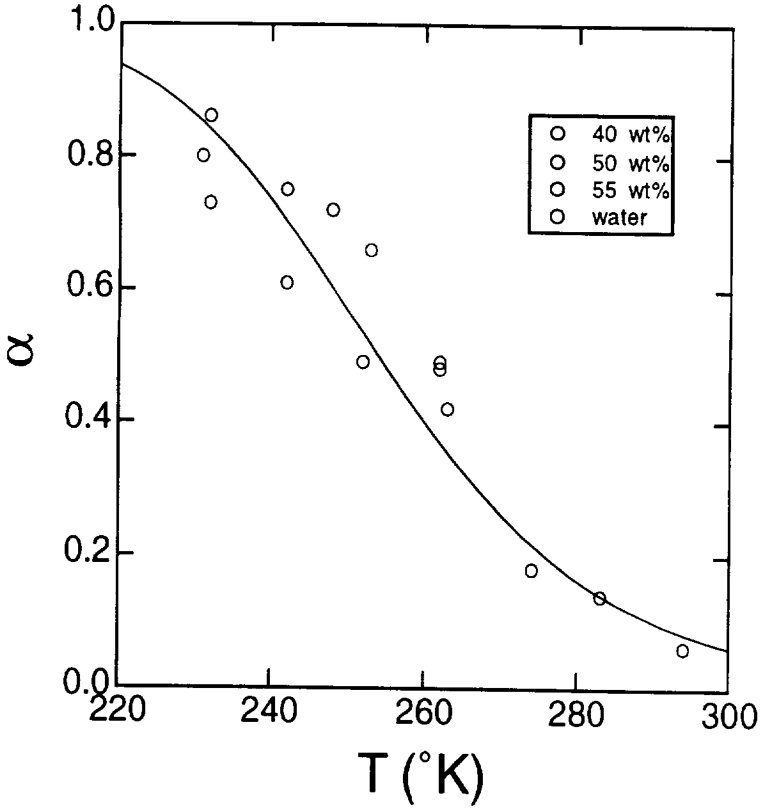

Figure 4. Temperature Dependence of HCl Mass Accommodation on Aqueous and Sulfuric Acid Solutions.

estimates of HCl solubility at room temperature (Watson et al., 1990). Note that the H values in Figure 3 are preliminary, since final analysis requires estimation of liquid diffusion coefficients.

Figure 4 plots the mass accommodation coefficient for HCl on aqueous and sulfuric acid solution between 230 and 290K (Van Doren et al., 1990; Robinson et al., 1992). These values are derived from correction for γ_{diff} as in equation (3), using the intercepts of the lines such as in Figure 2. Figure 4 shows that α(HCl) exhibits a strong negative temperature dependence, which gives values approaching unity at stratospheric temperatures. This is consistent with negative temperature dependencies we have measured for over 30 species (Jayne et al., 1991; Davidovits et al 1991).

The implication of these results for the stratosphere is summarized below:

a) When convolved with a volume fraction (L_c~$3x10^{-14}$) for background stratospheric aerosols (Hofmann and Solomon, 1989; Dye et al., 1992), even a Henry's law coefficient of 10^6 M/atm gives a negligible fraction of HCl dissolved in the aerosol ($HRTL_c$ ~ 10^{-6}). Only in the limit of volcanically perturbed aerosol at cold temperatures ($T < 200K$) could this fraction become significant. This small solubility can be used to explain the lack of observation of R4 in other laboratories (Hanson and Ravishankara, 1991b).

b) The plot of α in Figure 4 is the first direct measure of accommodation coefficients approaching unity. This is important for the stratosphere fast gas diffusion to submicron particles makes α rate limiting. It indicates that other results measuring reactivity on solid surfaces, which cannot experimentally resolve $\gamma > 0.3$, may indeed have reactivity probabilities approaching unity (Hanson and Ravishankara, 1991a). For HCl, the large value of α indicates that sulfuric acid aerosols will remain saturated in HCl.

Reactivity of N_2O_5

Figure 5 plots the uptake coefficients measured for this project together with results from other laboratories (Hanson and Ravishankara, 1991; Fried et al., 1993). Also included are previous room temperature results from our laboratory (Van Doren et al., 1991).

There are several points to note. First the logarithmic scale of Figure 5 has a narrow range, indicative of the weak dependencies of N_2O_5 reactivity on both temperature and sulfuric acid composition. Second, the values do converge on γ~0.12 in the stratospherically relevant range of 60-80 wt% at ~220K. The N_2O_5 chemistry has been distilled to that one number for current modeling (see for example, Rodriguez et al., 1992; Weisenstein, 1992).

However, careful examination of the results in Figure 5 indicate that N_2O_5 reactivity on sulfuric acid may be somewhat more complicated that currently thought. There is evidence of both a slight negative temperature dependence and a complex dependence on H_2SO_4 composition, with reactivity peaking on 60 wt% solution. Further experiments (particularly on 60 wt% solution) are in progress in our laboratory.

These issues are important because of the critical role of R1 in current stratospheric photochemical modeling. Analysis of 1991 aircraft measurements in and out volcanically perturbed aerosol layers over the Arctic are focusing on the rate and impact of R1.

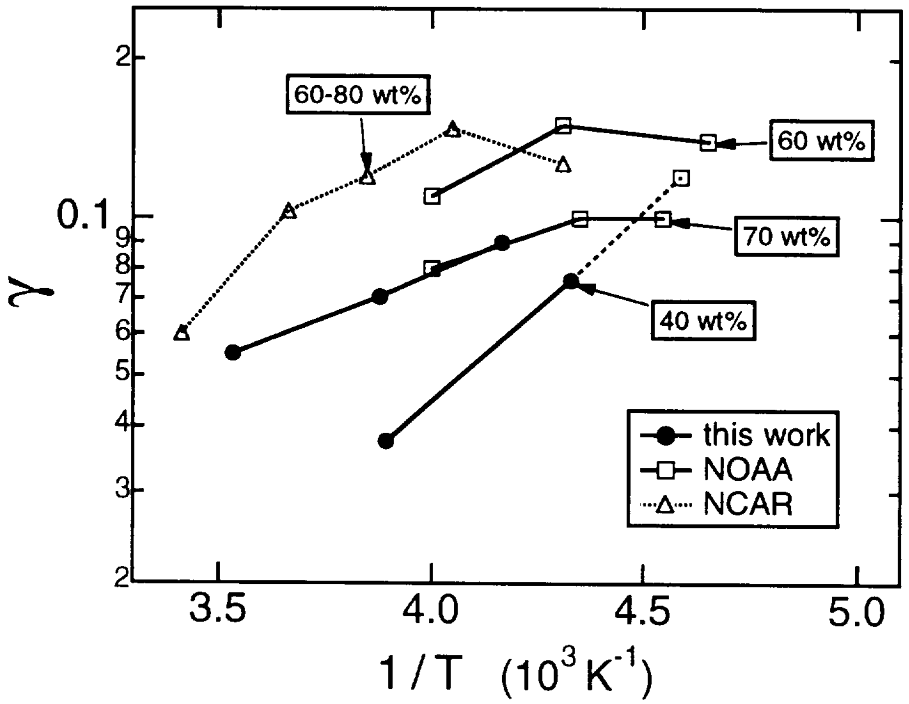

Figure 5. N_2O_5 Uptake on Sulfuric Acid Solution (NOAA: Hanson and Ravishankara, 1990; NCAR: Fried et al., 1993)

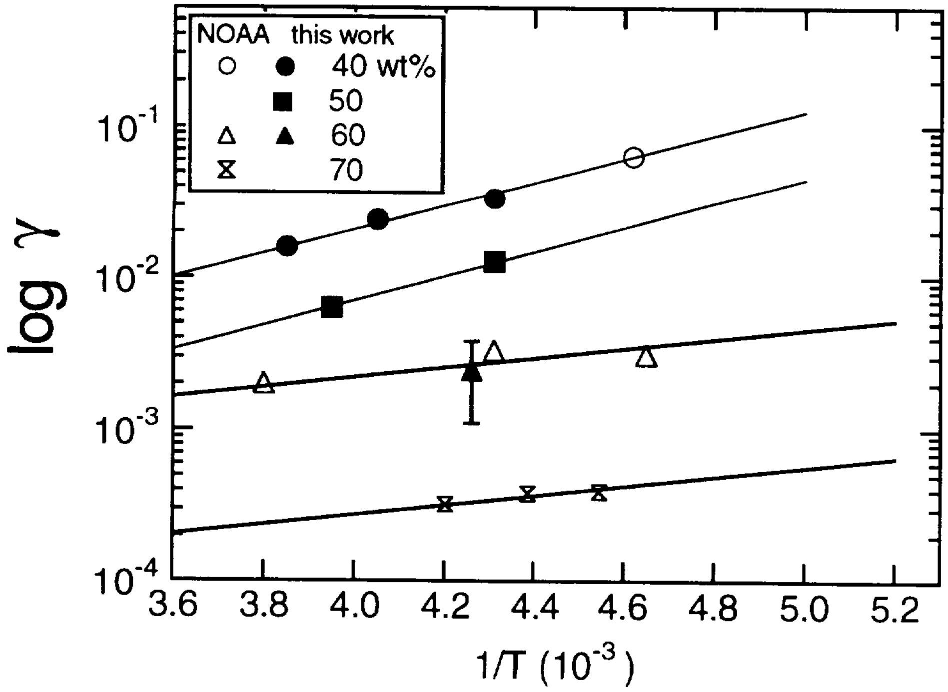

Figure 6. $ClONO_2$ Uptake on Sulfuric Acid Solution (NOAA: Hanson and Ravishankara, 1990)

Reactivity of $ClONO_2$

Figure 6 plots uptake coefficients measured for the reactivity of $ClONO_2$ on liquid sulfuric acid surfaces. Results from this project are displayed together with those of Hanson and Ravishankara (1991). Overall the agreement between the two sets of data are very good.

In contrast to N_2O_5, $ClONO_2$ reactivity has a strong dependence on sulfuric acid composition as has been previously reported (Tolbert et al., 1988; Hanson and Ravishankara, 1991b). In addition, our new results indicate that there may also be a significant temperature dependence, particularly on 40 wt% solution. This is potentially relevant to near-polar stratospheric conditions where sulfuric acid aerosols at T~195K are diluted to 40wt%. Reaction rates of $\gamma \sim 0.1$, as extrapolated on Figure 6, indicate that R2 could play a significant role in cold stratospheric chemistry.

The values plotted in Figure 6 are preliminary as final analysis of H_2SO_4 droplet surface composition and temperature is not complete.

Modeling Stratospheric Heterogeneous Chemistry

The uptake coefficients for N_2O_5 and $ClONO_2$ probably can be described in terms of a reactivity coefficient (Worsnop et al, 1989)

$$\gamma_{rxn} = 4HRT\,(D_l k_{rxn})^{1/2} / c$$

where k_{rxn} is the rate of reaction (s^{-1}) of the dissolved species in solution. This expression implies that one must know both the solubility and reactivity of species in solution in order to fully understand the mechanism. For N_2O_5 and $ClONO_2$, the lack of any observed time dependence in the millisecond droplet experiments indicates that $k_{rxn} > 10^3\ s^{-1}$. The dependencies on temperature and composition presumably convolve the separate dependencies of H and k_{rxn}. For N_2O_5 in particular, it is thus not surprising that the observed γ apparently has such a complex dependence on those parameters.

For the $ClONO_2$ + HCl reaction, which probably involves the solution phase reaction of HOCl(s) and HCl(s) (Hanson and Ravishankara, 1992), krxn can be expressed in terms of rate coefficient (k_l) for liquid phase reaction, $k_l[HCl(s)]$, where $[HCl(s)] = [HCl(g)]H_{HCl}RT$. Thus, the H_{HCl} plotted in Fig. 3 can be seen to be rate limiting for heterogeneous HCl reactivity.

This is an important point in applying these results to the stratosphere. The definition of γ_{rxn} (see eqn. (1)) and its direct application to photochemical kinetics assume that heterogeneous reaction rates are surface area limited. This is definitely true in the lab; however, for small aerosol particles in the stratosphere the dissolved gas in the particle may saturate at n_gHRT. Then the rate of heterogeneous processing of the trace gas is given by L_cHRTk_{rxn}.

Overall, detailed modeling such as has been done for tropospheric cloud processing (Chameides, 1984; Schwartz, 1986; Jacob, 1986) is required to at a minimum determine the parameterization required for appropriate inclusion of heterogeneous chemistry in photochemical models (Kawa et al., 1992b). The detailed uptake results reported are essential for that analysis.

VAPOR PRESSURES OF HNO_3 / H_2O HYDRATES

Satellite observations of Type I PSCs first indicated that clouds could condense over the pole at temperatures higher than the ice frost point (McCormick et al., 1982; Steele et al., 1993). Based on analysis and extrapolation of higher temperature phase diagrams to stratospheric conditions, various groups identified these clouds as hydrates of nitric acid (Crutzen and Arnold, 1986; Toon et al., 1986). Laboratory measurements then identified nitric acid trihydrate (NAT) as the most stable hydrate under stratospheric conditions (Hanson and Mauersberger, 1988a; 1988b). In situ, aircraft measurements of NOy and particles in Type I PSCs also indicated that they continued HNO_3 (Fahey et al., 1989).

The precise identification of Type I PSCs as NAT still was largely based the consistency of HNO_3 / H_2O vapor pressures and temperature with the one laboratory measurement of the NAT phase diagram (Hanson and Mauersberger, 1988). Meanwhile, Ritzhaupt and Devlin (1991) and Koehler et al. (1992) observed nitric acid dihydrate (NAD) in addition to NAT via FTIR thin film spectroscopy. Furthermore, careful analysis of aircraft observations of total NO_y and aerosol particles indicated that PSCs actually form at temperatures 2-4K colder than predicted by the equilibrium NAT phase diagram (Dye et al., 1992). Moreover, there seems to be a difference between Arctic and Antarctic observations (Kawa et al., 1992a).

Taken together, these observations suggest the identification of Type I PSCs is not entirely clear. More generally, a better understanding of PSC microphysics is clearly required for prediction of future PSC climatology. This is particularly important in proposed HSCT flight corridors in which elevated H_2O and HNO_3 vapor densities could enhance PSC nucleation. At tropical and mid latitudes, this could be a critical issue, since Cl_x activation in the presence of sunlight can significantly deplete ozone.

In what follows we summarize our measurements of HNO_3 / H_2O vapor pressures using tunable infrared diode laser spectroscopy. The goal was to confirm and extend existing measurements of the HNO_3 / H_2O phase diagram. A detailed discussion of these results has been published (Worsnop et al., 1993).

Optical Measurements of HNO3 / H2O Vapor Pressures

A schematic of the apparatus is shown in Figure 7. A multiple pass Herriott cell (40 passes x 50 cm/pass; 7.6-cm diameter gold-coated mirrors; see McManus and Kebabian, 1990) was suspended vertically in a 12-liter vacuum chamber constructed of gold-plated stainless steel and glass coated with $C_6F_{13}CH_2CH_2Si(OEt)_3$ (Petrarch Systems) (see Fig. 1). The optical cell is coupled to an infrared tunable diode laser system that was tuned to appropriate vibrational/rotational lines of H_2O and HNO_3. Partial pressures were determined by fitting Gaussian line profiles for 12 HNO_3 lines and 1 H_2O line between 1339.97 and 1340.18 cm^{-1}, with line strengths derived from recent measurements (Rothman et al., 1992; May and Webster, 1987). Detection limits were $\sim 10^{-7}$ torr for HNO_3 and $[HNO_3]/50$ for H_2O, limited by interference fringes for HNO_3 and by a weak HNO_3 feature for H_2O. Details of the diode laser system and data acquisition/analysis are discussed in Worsnop et al. (1992).

Sample temperatures were regulated between 190 and 230 K by flowing cold nitrogen gas onto a brass button epoxied to the cell exterior 20 cm below the detection region. Solid phases were condensed on the glass surface above the button by cooling mixtures of gaseous H_2O and HNO_3 or by adding gaseous H_2O or HNO_3 to a cold sample. The thickness of the condensed layer varied between 5 and 50 μm, estimated from the amount of gas phase H_2O and HNO_3 which condensed. Button temperature could be regulated with a precision of ±0.2 K (accuracy approximately ±0.4 K), as confirmed by comparing H_2O vapor pressures over ice to literature values (Jansco et al., 1970). Cell temperature above the cold point was set to 273 K for most experiments. Heating or

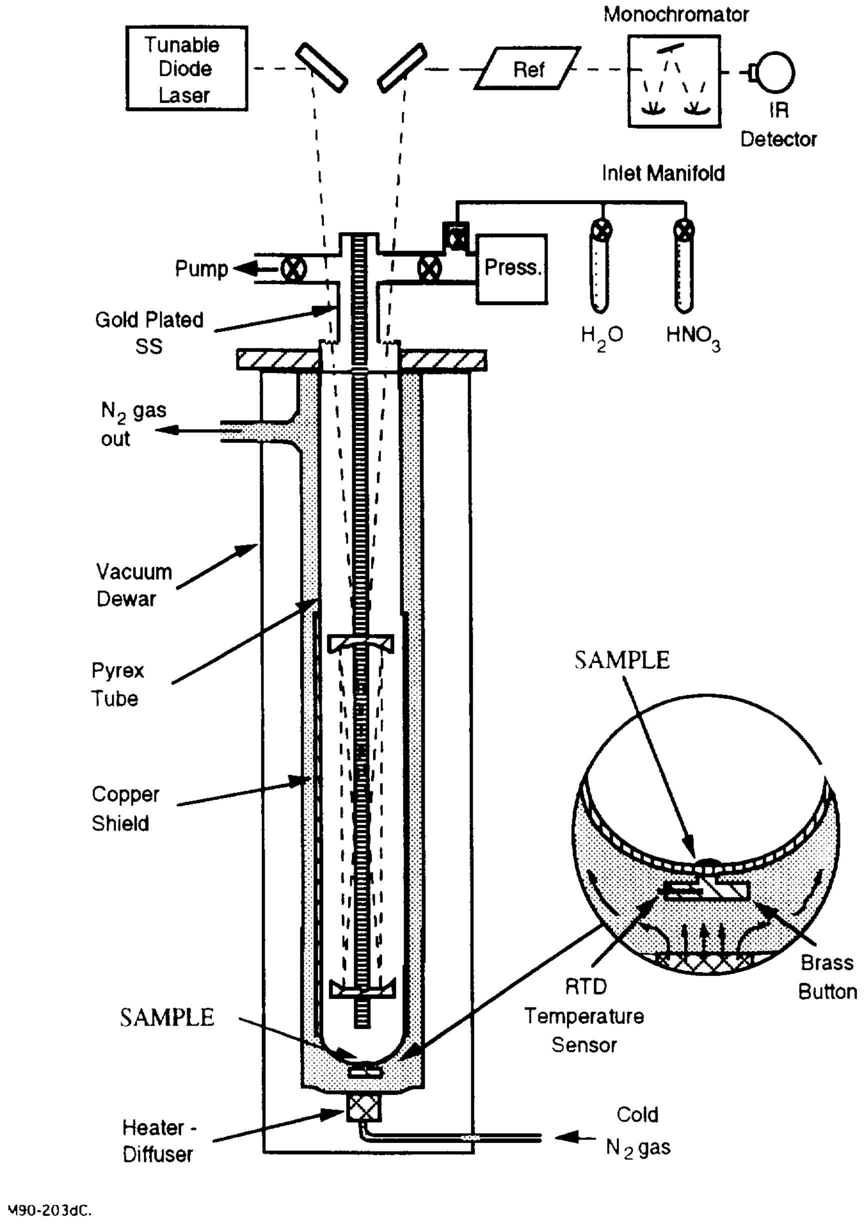

Figure 7. Schematic of Vapor Pressure Apparatus

cooling the Herriott cell between 240 and 295 K had no measurable effect on vapor pressures, indicating negligible influence of gases adsorbed on chamber walls.

This technique has several specific advantages compared to other experiments:

a) Gas density measurements are absolute, with uncertainties dependent only on the accuracy of the linestrengths of the molecular transitions.

b) The cell is static. Vapor pressures over a given sample can be observed for days or even weeks. Cell construction is ultrahigh vacuum compatible with inner chamber materials composed only of gold plated stainless steel and glass covered with a monolayer teflon-like coating.

c) Temperature control. Independent control of cell wall and cold spot temperatures can distinguish wall adsorption vapor pressures over sample versus cell wall adsorption.

Experimental procedures first condensed a substrate of well defined composition as described above;then a thin (1 to 20 μm) surface layer was condensed by adding additional HNO_3 and/or H_2O vapor. Measurements of the time evolution of the H_2O and HNO_3 vapor pressures identified different hydrates via vapor pressures following the Gibbs-Duhem equation

$$d(\ln p_{HNO_3})/\ d(\ln p_{H_2O}) = -n \qquad (1)$$

where n is the H_2O/HNO_3 ratio in the solid phase. Experiments on a time scale of days resolved slow, diffusion limited mixing of layers within the condensed sample. The NAT phase diagram was confirmed and that of NAD determined for the first time. Moreover, the long time duration experiments were clearly able to distinguish the existence of metastable NAD in preference to more stable NAT under temperature and vapor pressure conditions near to those found in the polar stratosphere.

Nitric Acid Hydrate Phase Diagram

Detailed results have been discussed in Worsnop et al. (1993). A summary is presented here. Overall, results are summarized in Fig. 8, which plots the temperature dependence of the equilibrium constants of the hydrates of nitric acid, defined according to the equation

$$K_n = p_{HNO_3}\left(p_{H_2O}\right)^n \qquad (2)$$

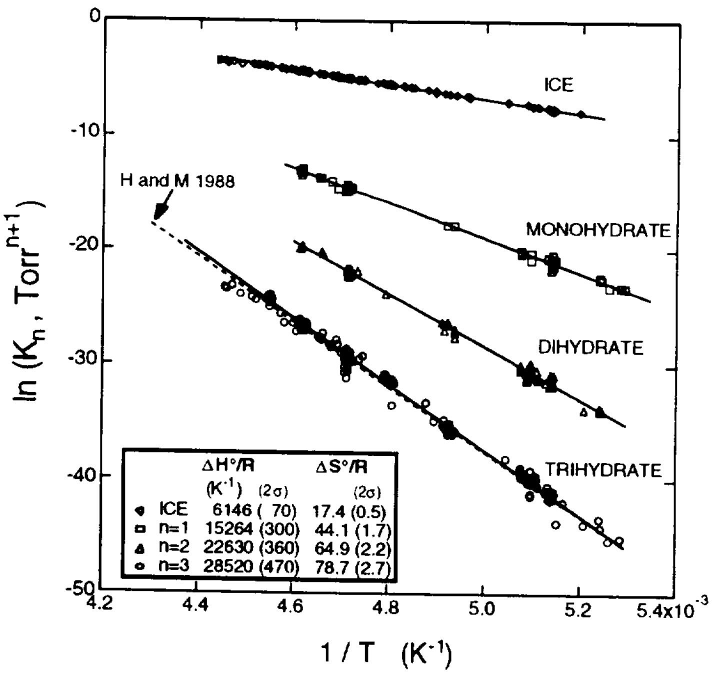

Figure 8. Equilibrium constants for nitric acid hydrates (Worsnop et al., 1993). Dashed line for NAT from Hanson and Mauersberger (1988a).

for (n=0,1,2,3), where pressures are in given in atmospheres, i.e. K_n has units of atm^{n+1}. Standard enthalpy and entropy values (inset in Fig. 8) for the vapor to solid phase transitions are obtained from the slopes and intercepts of the linear least square fits.

There are several points to be noted concerning the results of Fig. 8:

(a) The line for H_2O pressures over ice (n=0) was used to calibrate the cold spot temperature using literature values for the vapor pressure over ice (Jansco et al., 1970).

(b) The lines for nitric acid trihydrate (NAT) and monohydrate (NAM) agree very well with previous measurements. In particular, the NAT data is excellent agreement with Hanson and Mauersberger (1988a), especially over the temperature range of their experiments (190-205K), confirming their determination of NAT as the most stable phase under stratospheric conditions.

(c) The dihydrate (NAD) line represents the first determination of its thermodynamics. NAD is only slightly less stable than NAT under stratospheric conditions. This is consistent with the observation of NAD in thin films FTIR spectroscopy (Koehler et al., 1992).

The most significant new result is the determination that NAD is only slightly less stable than NAT under stratospheric conditions. This can be seen in Fig. 9 which displays the observation of metastable NAD at 196K. Fig. 9 involved an experiment in which HNO_3 vapor was added to an NAT substrate. This addition formed NAD which persisted for about a half hour, when NAT nucleated. The data in Fig. 9 combines four such experiments.

Several points are to be emphasized in Fig. 9:

(a) NAT is the most stable phase under stratospheric conditions. In Fig. 9 the stability region for NAD lies outside the range of the stratospheric box while the 196K NAT stability line crosses its right upper corner.

(b) Both NAT and NAD can form at temperatures higher than the ice frost point in the stratosphere. This result, in agreement with Hanson and Mauersberger (1988) for NAT, confirms that Type I PSCs are likely composed of nitric acid hydrates.

(c) Metastable NAD can exist in preference to the slightly more stable NAT.

(d) A saturation ratio of about 8 in HNO_3 vapor relative to equilibrium NAT is required to nucleate NAT. The formation of NAT in Fig. 9 matches such a saturation ratio and was a general result of all the vapor pressure experiments (Worsnop et al., 1993).

These results have significant implications for PSC microphysics. First, the saturation ratio of 8 in HNO_3 vapor for NAT nucleation may explain the 2-4K gap in the threshold for PSC appearance observed in Arctic field observations (Kawa et al., 1992a). In fact, the NAD phase diagram also correlates very well with those observations. More experiments are required to investigate nitric acid hydrate nucleation on liquid sulfuric acid surfaces that simulate the background aerosols that provide the nucleation substrates in the stratosphere.

As one final example of the importance of PSC microphysics, one should note the formation of metastable NAD has significant implications for denitrification in the stratosphere. The mechanism involving "HNO_3 condensation on falling ice particles" becomes much more likely in the presence

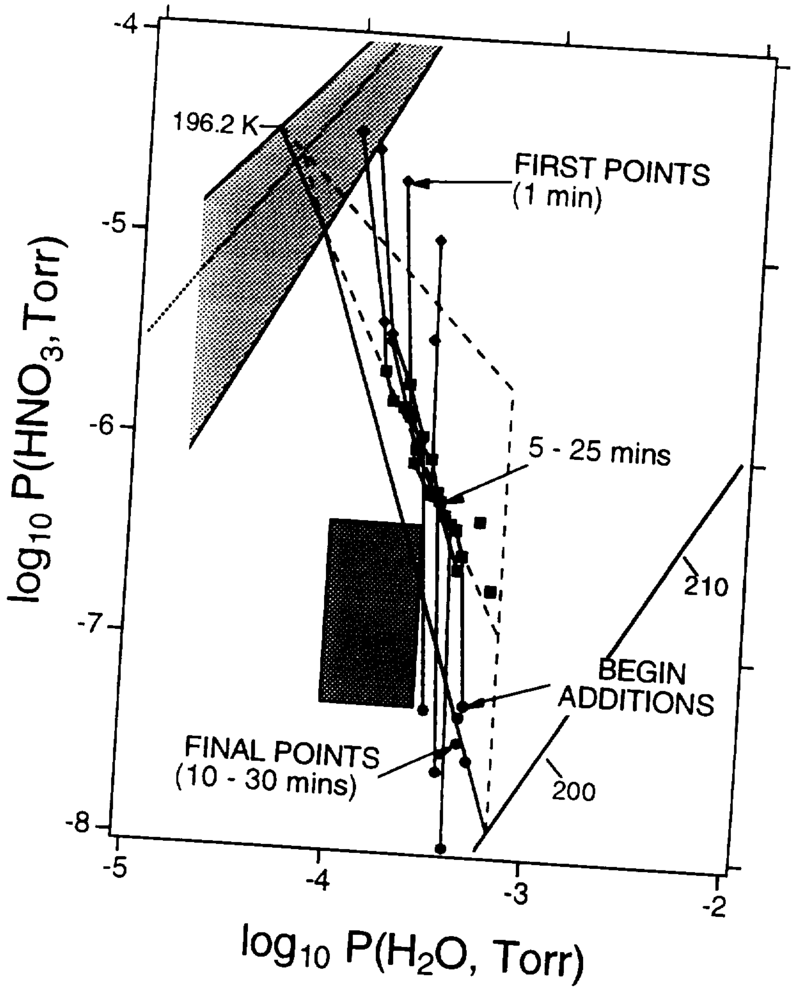

Figure 9. HNO_3 / H_2O Phase Diagram. Shaded region at upper left is NAD stability region. Solid diagonal line shows NAT stability at 196K, which crosses box representing stratopsheric conditions. Dashed lines show metastable NAD, NAM and ice phases at 196K. Data points follow metastable NAD line as described in text (see Worsnop et al., 1993).

of NAD (Wofsy et al., 1990). The key point is that aerosol nucleation is a non-equilibrium phenomenon, which requires a full understanding of the thermodynamics of the condensed phases.

Relevance to Stratospheric Flight

The overall goal for the HSRP program is to integrate variations in aerosol composition and distribution with the heterogeneous reaction chemistry represented by R1-R4.

The growing diversity of aerosol observations and apparent complexity of NAT nucleation is very relevant to the modeling of potential chemical perturbations due to aircraft emissions. Those emissions are projected to occur in the center of the background sulfate layer. Especially at lower temperatures at lower altitudes (< 20 km) near the tropopause and at higher latitudes in the winter, emission of H_2O vapor and condensation nuclei could significantly enhance aerosol formation, since background conditions there are already very close to NAT condensation predictions (Hamill and Fiocco, 1988). Combined with reports of possible observation of local ozone perturbations due to direct interaction with Arctic and Antarctic aerosols (Hoffmann, 1989; Hoffmann et al., 1989; Fiocco et al., 1989), it is important to quantitatively understand the vapor pressure diagrams for prediction of aerosol formation and growth.

REFERENCES

Chameides, W.L., "The Photochemistry of A Remote Marine Stratiform Cloud," J. Geophys. Res. 89, 4739 (1984).

Crutzen, P.J. and F. Arnold, Nature 324, 651 (1986).

Davidovits, P, J.T. Jayne, S.X. Duan, D.R. Worsnop, M.S. Zahniser and C.E. Kolb, "Uptake of Gas Molecules by Liquids: A Model" , J.Phys. Chem. 95, 6337 (1991),

Dye, J.E., Baumgardner, D., Gandrud, B.W., Kawa, S.R., Kelly, K.K., Lowenstein, M., Ferry, G.V. and Gary, B.L., "Particle Size Distributions in Arctic Polar Stratospheric Clouds: Growth and Nucleation of Sulfuric Acid Droplets and Implicatins for Cloud Formation," J. Geophys. Res. 97, 8015 (1992).

Fahey, D.W., Kelly, K.K., Ferry, G.V., Poole, L.R., Wilson, J.C., Murphy, D.M., Loewenstein, M. and Chan, K.R., "In Situ Measurements of Total Reactive Nitrogen, Total Water, and Aerosol in a Polar Stratospheric Cloud in the Antarctic," J. Geophys. Res. 94, 11, 299 (1989).

Fiocco, G., Komhyr, W.D., and Fua, D., "Is Ozone Destroyed During the Antarctic Winter in the Presence of Polar Stratospheric Clouds?," Nature, 341, 426 (1989).

Hamill, P., and Fiocco, G., "Nitric Acid Aerosols at the Tropical Tropopause," J. Geophys. Res. 15, 1189-1192, 1988.

Hanson, D., and Mauersberger, "Laboratory Studies of the Nitric Acid Trihydrate Implications for the South Polar Stratosphere," Geophys. Res. Lett. 15, 855-858, (1988a).

Hanson. D., and Mauersberger, "Vapor Pressures of HNO_3/H_2O Solutions at Low Temperatures," J. Phys. Chem. 92, 6167-6170 (1988b).

Hanson, D., and A.R. Ravishankara, "The Reaction Probabilities of $ClONO_2$ and N_2O_5 on Polar Stratopsheric Cloud Materials", J. Geophys. Res. 96, 5081 (1991a).

Hanson, D., and A.R. Ravishankara, "The Reaction Probabilities of $ClONO_2$ and N_2O_5 on 40 to 75% Sulfuric Acid Solutions", J. Geophys. Res. 96, 17,307 (1991b).

Hanson, D., and A.R. Ravishankara, "Invesitgation of the Reactive and Nonreactive Processes Involving ClONO2 and HCl on Water and Nitric Acid Doped Ice", J. Phys. Chem. 96, 2682 (1992).

Hofmann, D.J., "Direct Ozone Depletion in Springtime Antarctic Lower Stratospheric Clouds," Nature, Vol. 337, (1989).

Hofmann, D.J., Deshler, T.L., Aimedieu, P., Matthews, W.A., Johnston, P.V., Kondo, Y., Sheldon, W.R., Byrne, G.J., and Benbrook, J.R., "Stratospheric Clouds and Ozone Depletion in the Arctic During January 1989," Nature, Vol. 340, (1989).

Hofmann, D.J., and Solomon, S., "Ozone Destruction Through Heterogeneous Chemistry Following the Eruption of El Chichon," J. Geophys. Res. 94, 5029 (1989).

Jacob, D.J., "Chemistry of OH In Remote Clouds and Its Role In the Production of Formic Acid and Peroxymonosulfate," J. Geophys. Res. 91, 9807 (1986).

Jansco G., J. Pupezin, W.A. van Hook, J. Phys. Chem. 74, 2984 (1970).

Jayne, J.T., S.X. Duan, P. Davidovits, D.R. Worsnop, M.S. Zahniser and C.E. Kolb,"Uptake of Gas-Phase Alcohol Molecules and Organic Acids by Water Surfaces", J.Phys Chem. 95, 6329 (1991),

Kawa, S.R., D.W. Fahey, Kelly, K.K., J.E.Dye, D. Baumgardner, B.W. Gandrud, M.Lowenstein, G.V.Ferry and K.R.Chan, "The Arctic Polar Stratospheric Cloud Aerosol: Aircraft Measurments of Reactive Nitrogen, Total Water, and Particles", J. Geophys. Res. 97, 7905 (1992).

Kawa, S.R., et al., "Simulation of Stratopsheric NO_x/NO_y Based on ER-2 Measurements", Abstract, AGU Fall Meeting, EOS Supplement, 134 (October, 1992b)

Koehler, B.G., Middlebrook, A.M. and Tolbert, M.A., "Characterization of Model Polar Stratospheric Cloud Films Using Fourier Transform Infrared Spectroscopy and Temperature Programmed Desorption," J. Geophys. Res. 97, 8065 (1992).

R.D. May and C.R. Webster, J. Quant. Spec. Rad. Transf. 38, 5 (1987).

McCormick, M.P., Steele, H.M., Hamill, P., Chu, W.P., and Swissler, T.J., "Polar Stratospheric Cloud Sightings by SAM II," J. Atmos. Sci., 39, 1387-1397 (1982).

McManus, J.B. and P.L. Kebabian, "Narrow Optical Interference Fringes for Certain Setup Conditions in Multipass Absorption Cells of the Herriott Type," App. Optics 29, 898 (1990).

Mozurkewich, M. and Calvert, J.G., "Reaction Probability of N_2O_5 on Aqueous Aerosols," J. Geophys. Res. 93, 15889 (1988).

Ritzhaupt, G. and Devlin, J.P., "Infrared Spectra of Nitric and Hydrochloric Acid Hydrate Thin Films," J. Phys. Chem. 95, 90-95 (1991).

Rodriguez, J.M., M.K.W.Ko and N.D.Sze, "Role of Heterogneous Conversion of N_2O_5 on Sulphate aerosols in global ozone losses", Nature 352, 134 (1991).

Rothman, L.S. et al., J. Quant. Spec. Rad. Transf. 48, 469 (1992).

Schwartz, S.E., "Mass-Transport Considerations Pertinent to Aqueous Phase Reactions of Gases in Liquid-Water Clouds," in Chemistry of Multiphase Atmospheric Systems, NATO ASI Series, Vol. G6, ed. W. Jaeschke, Springer-Verlag (New York), pp 415-471 (1986).

Steele, H.M., Hamill, P., McCormick, M.P., and Swissler, T.J., "The Formation of Polar Stratospheric Clouds," J. Atmos. Sci. 40, 2055 (1983).

Tolbert, M.A., Rossi, M.J., and Golden, D.M., "Heterogeneous Interactions of $ClONO_2$, HCl, and HNO_3 with Sulfuric Acid Surfaces at Stratospheric Temperatures," Geophys. Res. Lett. 15, 847 (1988b). Values recently revised, Tolbert, M.A. (1989).

Toon, O.B., P. Hamill, R.P. Turco, and J. Pinto, "Condensation of HNO_3 and HCl in the winter polar stratosphere", Geophys. Res. Lett. 13, 1284 (1986).

Van Doren, J.M., Watson, L.R., Davidovits, P., Worsnop, D.R., Zahniser, M.S., and Kolb, C.E., "Temperature Dependence of the Uptake Coefficient for HCl, HNO_3, and N_2O_5 On Water Droplets," J. Phys. Chem., 94, 3265 (1990).

Van Doren, J.M., Watson, L.R., Davidovits, P., Worsnop, D.R., Zahniser, M.S., and Kolb, C.E., "Uptake of N_2O_5 and HNO_3 by Aqueous Sulfuric Acid Droplets," J. Phys. Chem. 95, 1684 (1991).

Watson, L., Van Doren, J.M., Davidovits, P., Worsnop, D., Zahniser, M.S., and Kolb, C.E., "Uptake of HCl Molecules By Aqueous Droplets As a Function of Sulfuric Acid Concentration," J. Geophys. Res. 95, 5631 (1990).

Weisenstein, D.K., J.M.Rodriguez, M.K.W.Ko and N.D.Sze, "Impact of Heterogeneous Chemistry on Model Calculated Oxone Change due to High Speed Civil Transport Aircraft," Geophy. Res. Lett. 18, 1991, (1991).

Wofsy, S.C., Salawitch, R.J., Yatteau, J.H. McElroy, M.B., Gandrud, B.W., Dye, J.E. and Baumgardner, D., "Condensation of HNO_3 of Falling Ice Particles: Mechanisms for Denitrification of the Polar Stratosphere," Geophy. Res. Lett. 17, 449-452, (1990).

Worsnop, D.R., Zahniser, M.S., Kolb, C.E., Gardner, J.A., Watson, L.R., Van Doren, J.M., Jayne, J.T., and Davidovits, P., "The Temperature Dependence of Mass Accommodation of SO_2 and H_2O_2 On Aqueous Surfaces," J. Phys. Chem. 93, 1159 (1989).

Worsnop, D.R., Zahniser, and D.N. Nelson, "Chemical Kinetic Studies of Atmospheric Reactions Using Tunable Diode Infrared Spectroscopy," SPIE 18, 1715 (1992)

Worsnop, D.R., Fox, L.E., Zahniser, M.S., and Wofsy, S.C., "Vapor Pressures of Nitric Acid Hydrates: Implications for Stratospheric Clouds," Science 259, 71 (1993).

REPORT DOCUMENTATION PAGE

Form Approved
OMB No 0704-0188

1. AGENCY USE ONLY *(Leave blank)*

2. REPORT DATE
July 1993

3. REPORT TYPE AND DATES COVERED
Contractor Report

4. TITLE AND SUBTITLE
Stratospheric Aircraft Exhaust Plume and Wake Chemistry

5. FUNDING NUMBERS
C NAS1-19161
WU 537-01-20-01

6. AUTHOR(S) R.C. Miake-Lye, M. Martinez-Sanchez, R.C. Brown, C.E. Kolb, D.R. Worsnop, M.S. Zahniser, G.N. Robinson J.M. Rodriguez, M.K.W. Ko, R-L. Shia, N.D. Sze, C.W. Heisey, L. Fox, S.C. Wofsy, and P. Davidovits

7. PERFORMING ORGANIZATION NAME(S) AND ADDRESS(ES)
Aerodyne Research, Inc.
45 Manning Road
Billerica, MA 01821

8. PERFORMING ORGANIZATION REPORT NUMBER
ARI-RR-1006

9. SPONSORING/MONITORING AGENCY NAME(S) AND ADDRESS(ES)
National Aeronautics and Space Administration
Langley Research Center
Hampton, VA 23681-0001

10. SPONSORING/MONITORING AGENCY REPORT NUMBER
NASA CR-191495

11. SUPPLEMENTARY NOTES
Langley Technical Monitor: William L. Grose

12a. DISTRIBUTION/AVAILABILITY STATEMENT
Unclassified-Unlimited

Subject Category 46

12b. DISTRIBUTION CODE

13. ABSTRACT *(Maximum 200 words)*

This report documents progress to date in an ongoing study to analyze and model emissions leaving a proposed High Speed Civil Transport (HSCT) from when the exhaust gases leave the engine until they are deposited at atmospheric scales in the stratosphere. A kinetic condensation model has been implemented to predict heterogeneous condensation in the plume regime behind an HSCT flying in the lower stratosphere. Simulations were performed to illustrate the parametric dependence of contrail droplet growth on the exhaust condensation nuclei number density and size distribution. Model results indicate that the condensation of water vapor is strongly dependent on the number density of activated CN. Incorporation of estimates for dilution factors into a Lagrangian box model of the far-wake regime with scale-dependent diffusion indicates negligible decrease in ozone and enhancement of water concentrations of 6-13 times backgound, which decrease rapidly over 1-3 days. Radiative calculations indicate a net differential cooling rate of the plume about 3K/day at the beginnng of the wake regime, with a total subsidence ranging between 0.4 and 1 km. Results from the Lagrangian plume model have been used to estimate the effect of repeated superposition of aircraft plumes on the concentrations of water and NO_y along a flight corridor. Results of laboratory studies of heterogeneous chemistry are also described. Kinetics of HCl, N_2O_5 and $ClONO_2$ uptake on liquid sulfuric acid have been measured as a function of composition and temperature. Refined measurements of the thermodynamics of nitric acid hydrates indicate that metastable dihydrate may play a role in the nucleation of more stable trihydrates PSCs.

14. SUBJECT TERMS
Stratospheric chemistry, Ozone, Aircraft emissions, Stratospheric aircraft, High-speed civil transport, Contrail, Vortex wake

15. NUMBER OF PAGES
62

16. PRICE CODE

17. SECURITY CLASSIFICATION OF REPORT
Unclassified

18. SECURITY CLASSIFICATION OF THIS PAGE
Unclassified

19. SECURITY CLASSIFICATION OF ABSTRACT
Unclassified

20. LIMITATION OF ABSTRACT